Nanofabrication and Surface Characterization for Biosensors

Sabaa Rashid

Thesis submitted to the University of Ottawa
in partial Fulfillment of the requirements for the degree of

Master of Applied Science in Chemical Engineering

Department of Chemical and Biological Engineering
Faculty of Engineering
University of Ottawa

Abstract

This thesis is focused on surface characterization and nanofabrication techniques to be exploited potentially for use in biosensors and is divided into two articles. The first article presents an investigation of the non-specific adsorption of bovine serum albumin (BSA) labeled with fluorescein isothiocyanate (FITC) to microfluidic material surfaces through fluorescence microscopy. The tested and characterized material surfaces include the three commercially available grades of the fluoropolymer CYTOP (poly[perfluoro(4-vinyloxy-1-butene)]), M, A and S, as well as thermally grown silica on Si, and SU-8. In addition, surface roughness and surface wettability measurements were performed on the tested surfaces and related to the non-specific adsorption results. The lowest adsorption of BSA occurred on SU-8 likely due to its hydrophilicity, followed by S-grade CYTOP despite being hydrophobic.

The second article introduces a new nanofabrication process: helium ion beam lithography and liftoff. The process produces negligible proximity effects and exploits the higher resist sensitivity to helium ions compared to a conventional electron beam. The fabrication process targeted the realisation of nanoantenna arrays on fused silica substrates; however, the process was successfully applied to multiple substrates including Si, silver films on Si and MgO substrates with minimal alteration. The fabricated structures imaged via helium ion microscopy and AFM showed good overall agreement with the target layout dimensions. In addition, the optical transmittance response of the fabricated arrays was experimentally measured and compared to 3D-finite-difference time domain (FDTD) simulations revealing excellent agreement. Isolated gold lines, 20 nm thick and of width as small as 14 nm, were realised on Si, which matches the width achieved using state-of-the-art electron beam lithography systems.

Acknowledgments

I would like to express my ultimate gratitude to my research supervisor Dr. Pierre Berini who guided and encouraged me through his superb knowledge and wisdom. I truly appreciate all the fruitful discussions we had that helped improve my personal and professional skills. Moreover, I am thankful for the various opportunities he made available for me to work on various projects and with cutting-edge technology. Thank you very much for the financial support during my graduate studies.

I would also like to sincerely thank Dr. Oleksiy (Alex) Krupin, who was the reason why I joined this research group, for his valuable lessons in biosensing, advice and friendship. It was a great privilege to get trained, taught and supported by Anthony (Tony) Olivieri who was always available to help me in the lab. I would like to deeply thank you for all the serious and fun times I had with you, learning and laughing. I would like to express my special thanks to Dr. Choloong Hahn who trained me on our focused ion beam instrument (Rosie), to our lab staff Howard Northfield and Ewa Lisicka-Skrzek. I would like to thank Jesse Ward-Bond for introducing me to the NSA work and Maude Amyot-Bourgeois for introducing me to Rosie. I thank everyone who was and is part of our research group for their support and friendship.

And finally, I offer my heartfelt thanks to my parents and to Poosh for believing in me and endlessly supporting me. Thank you very much.

Table of Contents

Chapter 1 – Introduction

This chapter presents an overview of biosensing, optical plasmonic biosensors, characteristics and challenges in biosensors, and nanoantenna-based biosensors, as means to motivate and introduce the two articles in Chapters 2 and 3. These articles focus on the non-specific adsorption of proteins to microfluidic material surfaces, and a new fabrication process for the realisation of nanostructures, respectively.

1.1 Basics of biosensing

The earliest techniques used for sensing relied on animals, such as canaries in coal mines for detecting carbon monoxide gas. Such a practice remains in use today, for example, via the use of dogs to detect explosives and drugs. Although extremely sensitive and selective, the use of animals comes at a very high cost and represents a generally impractical solution to sensing. The multidisciplinary field of biosensing aims to develop transducer technologies that can report (bio)chemical interactions of interest. Biosensors nowadays are commonly used in biomedical diagnosis, environmental monitoring, food control, forensics, and biomedical research. A biosensor is an analytical device that generates an electronic signal selective and proportional to the amount of analyte present in a sample (usually a bodily fluid, such as blood, urine or saliva) [1]. The working principle of a biosensor is illustrated in Figure 1.

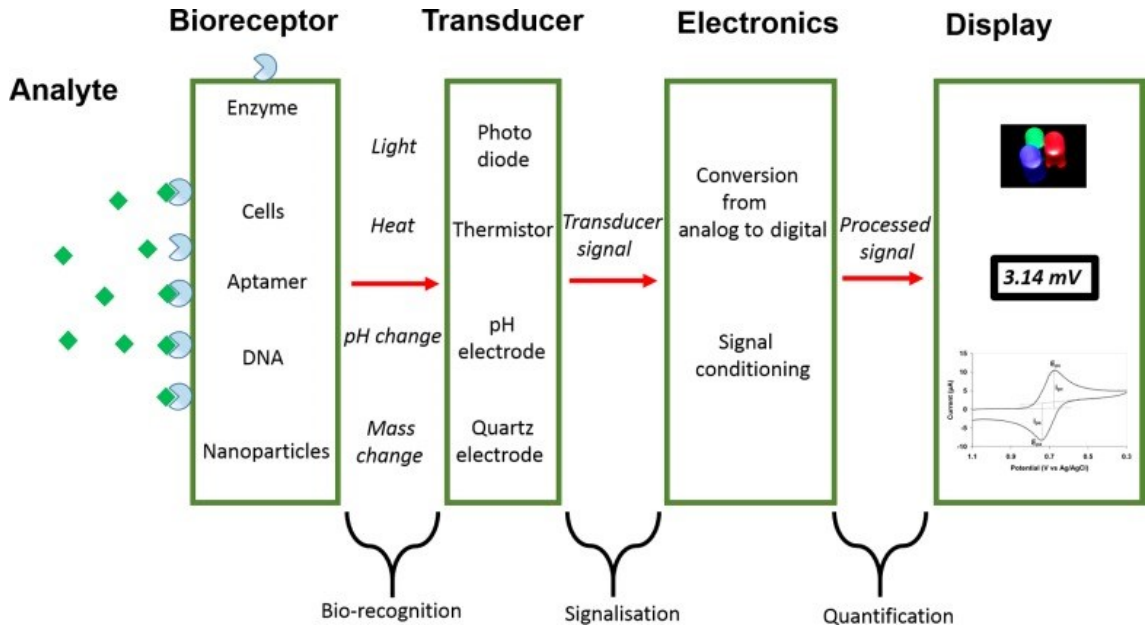

Figure 1. The working principle of a biosensor. Adapted from Introduction to biosensors [1] by N. Bhalla, P. Jolly, N. Formisano, and P. Estrela, with permission from Portland Press.

A biosensor aims to detect an analyte (*e.g.*, antigen) which is the targeted entity for detection, making use of a bioreceptor (*e.g.*, antibodies, enzymes and cells) that selectively binds to the target analyte, a transducer that converts the biochemical interaction embodied by the binding process between the analyte and the bioreceptor into a detectable electronic signal, followed by the output system involving electronics to process the transduced signal, amplifying it for display [2]. The binding process could be analyzed in terms of the change in electrical current, mass, temperature and light depending on the type of transducer used. The major types of biosensors include electrochemical, optical, and piezoelectric sensors. Electrochemical biosensors, which enable glucose monitoring for diabetes management, are based on the ability of some electroactive species to undergo redox reactions [3] in which electrons or ions are produced or consumed causing changes in current. The measured current can then be ascribed to the concentration of the electroactive species present in the sample, or their rate of generation or consumption [4].

Optical biosensors rely on the change in the phase, amplitude, polarization or frequency of the input light source in response to the binding process, which facilitates real-time, label-free and non-destructive detection, allowing for quantitative and kinetic measurements of biomolecular interactions [4]. The most studied type of optical biosensor is based on surface plasmon resonance (SPR), which will be discussed later in detail, in addition to long-range surface plasmon polariton (LRSPP) waveguide sensors.

Piezoelectric biosensors are based on detecting the changes in resonance frequency of an oscillating crystal due to biological interactions between the analyte and bioreceptor. The transducer in this biosensor is made of a piezoelectric material (*e.g.*, quartz). These materials generate an electric signal when mechanically stressed. The piezoelectric transducer is coated with the bioreceptor material which binds to the analyte, permitting the application of mechanical stress. Hence, the mass of the analyte adsorbed onto the surface of transducer can be calculated based on the changes in the resonant frequency [4].

1.2 SPR-based sensors

Surface plasmon resonance (SPR) is a charge density oscillation occurring at the interface of a metal and a dielectric material, coupled to an electromagnetic wave. Electrons in metals move freely along the metal lattice since they are loosely bound to the metal atoms, and are responsible for the high electric conductivity and optical reflectivity of metals [5]. These free electrons can be excited to generate propagating surface plasma waves along a metal-dielectric interface. Metal candidates for plasmonic applications include gold, silver, copper and aluminum [6]. However, the transducer is usually made of gold in SPR sensors because it is chemically stable, is ubiquitously studied for functionalization with self-assembled monolayers (SAMs) [7], and is

easily structured through lithographic techniques incorporating different deposition methods: sputtering, electro-deposition, and physical vapor deposition.

To excite surface plasmons, SPR sensors generally use a gold-coated glass prism in the Kretschmann-Raether configuration, arranged to monitor attenuated total reflectance when monochromatic light is reflected from the base of the prism beyond the critical angle (θ_c). At the SPR excitation angle (θ_1), most of the incident beam energy is transferred (coupled) to a surface plasmon wave localized at the gold-sensing fluid (gold-dielectric) interface; therefore, the intensity of the reflected light decreases significantly as shown in Figure 2. The SPR angle depends on the refractive indices of gold, the sensing fluid, and the bound analyte to bioreceptor adlayer that forms on the gold surface. When analyte molecules bind to the functionalized gold layer, the incident angle for coupling to surface plasmons changes, *i.e.*, θ_1 changes to θ_2, as shown in Figure 2. This shift is due to the change of the refractive index localized at the gold surface. The difference between the two angles represents the amount of analyte bound to the surface as shown in Figure 2. Monitoring the change in SPR angle with respect to time generates what is called a sensorgram which can be used to determine the amount of bound analyte, and the kinetics of association/disassociation between the analyte and bioreceptor [5].

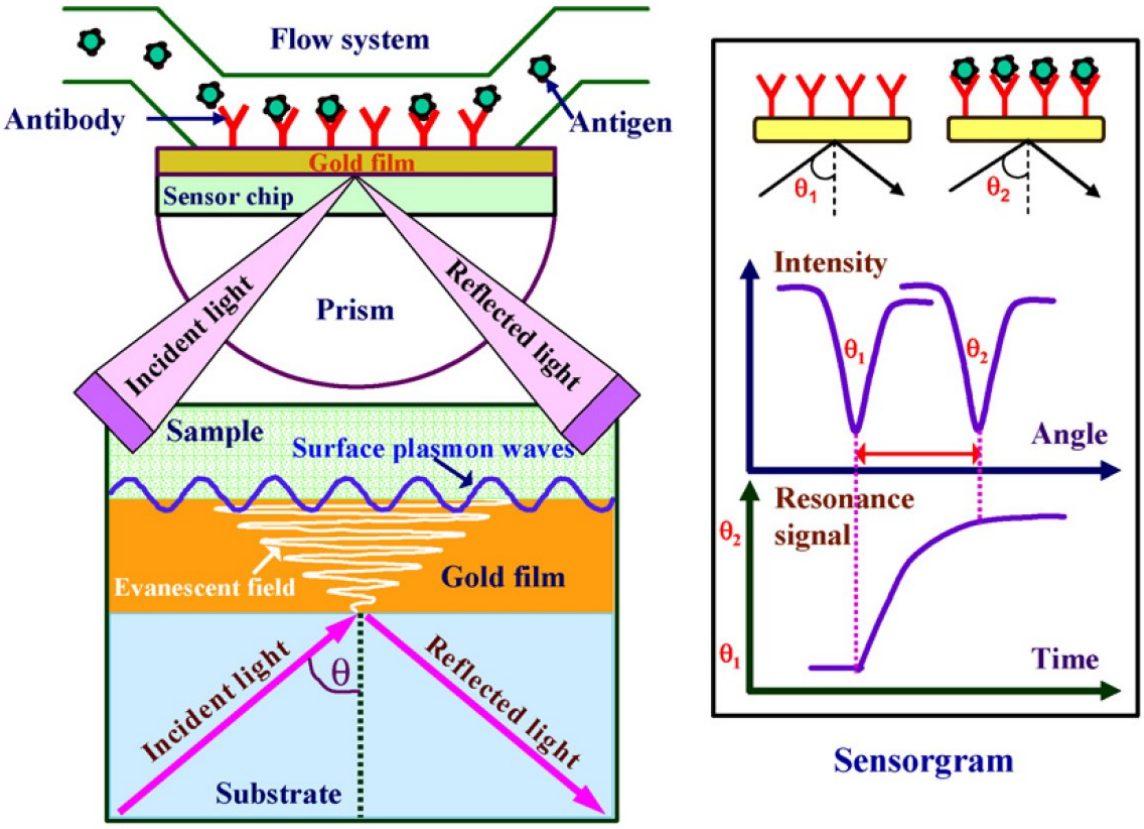

Figure 2. Schematic diagram of an SPR biosensor. Adapted from [5] with permission, *licence number* 4918401352951

1.3 Long range surface plasmon polariton (LRSPP)-based sensors

LRSPP are transverse magnetic (TM) plasmon waves propagating on thin metal stripes (waveguides) embedded in a dielectric material [7]. These structures can be used as attenuation-based biosensors. In this sensor, the functionalized gold waveguide is excited with a laser beam from one end and an optical power sensor is positioned on the other end to measure the power output. First a buffer solution is introduced into the sensor to establish a baseline signal, then when the analyte solution is introduced, the power output signal changes, revealing binding based on a change in the refractive index of the thin adlayer that grows on the surface of the gold waveguide [8]. A sensing setup is illustrated in Figure 3.

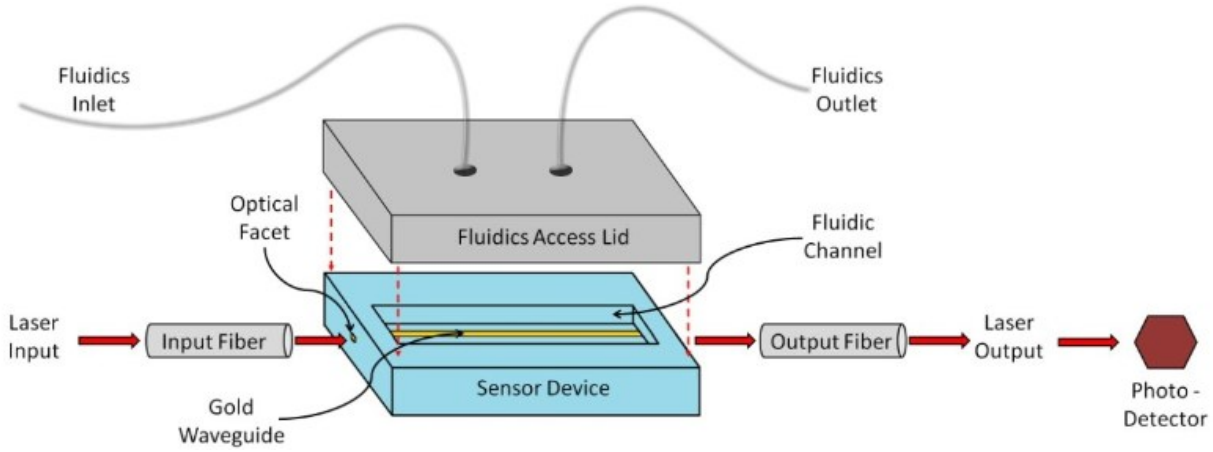

Figure 3. Schematic diagram of the sensing setup. Adapted from [9]

The fabrication process of this sensor involves the use of materials that have a refractive index close to that of water to maintain refractive index symmetry with respect to the metal stripe. Therefore, it is necessary for the material to closely match the refractive index of the sensing fluid, which is typically a biologically-compatible fluid such as phosphate buffered saline (PBS) having a refractive index close to that of water (~1.330). Good candidate dielectric materials to support the gold waveguide include Teflon and CYTOP fluoropolymers, which both have refractive indices close to that of water [7]. An LRSPP biosensor (Figure 4) is composed of a thin gold stripe of width 5 μm and thickness 35 nm, bounded by two thick layers of CYTOP as optical claddings. Fluidic channels are etched into the upper cladding to access the gold stripe and enable the flow of the sensing fluid. The fabrication process involves the preparation of a silicon substrate, spin-coating, optical lithography, metal deposition and etching of the fluidic channels [10]. This biosensor was used to demonstrate protein sensing using bovine serum albumin (BSA) [8], the selective capture of human red blood cells [11], the detection of leukemia markers in patient serum (in collaboration with Mt. Sinai Hospital, Toronto) using a functionalization strategy involving

Protein G and antibodies [12], and the detection of dengue NS1 antigen [13] (in collaboration with University of Malaya).

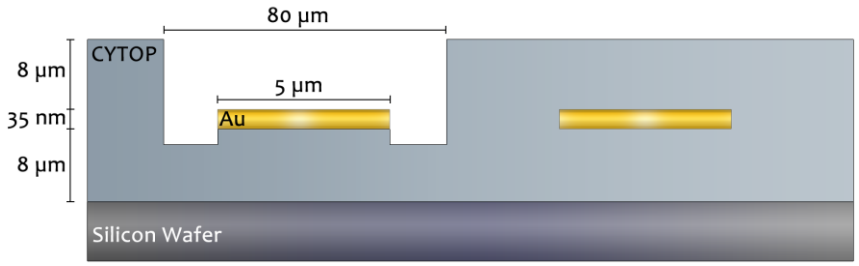

Figure 4. LRSPP biosensor composed of a gold waveguide embedded in CYTOP. Adapted from [9].

1.4 Characteristics and challenges in biosensors

Optimising the performance of a biosensor requires investigating five characteristics: selectivity, sensitivity, reproducibility, stability, and linearity. The biosensor selectivity towards the analyte is governed by the ability of the bioreceptor in detecting the analyte when present in a complex fluid that contains many other biomolecules and contaminants. The sensitivity of the sensor is described as the minimum possible concentration of the analyte present in a complex fluid that can be detected with high precision and accuracy. When repeating measurements, it is necessary to reproduce the same response which characterises the reproducibility of the sensor. The stability of the sensor requires a high-quality transducer and electronics to compensate for any disturbances in the biosensing setup such as fluctuations in temperature that may influence the sensor performance. The detection limit corresponds to the smallest change in the analyte concentration that causes a noticeable change in the sensor's response [1].

Non-specific adsorption is problematic in biosensors causing degraded performance in terms of selectivity, sensitivity, and reproducibility. To achieve a better performance, both the transducer surface (*e.g.*, waveguide in an optical sensor) and the surrounding material (*e.g.*,

cladding in an optical sensor) should be impervious to non-specific adsorption [14,15]. Hence, Chapter 2 investigates the non-specific adsorption of proteins to different material surfaces that are used in the fabrication of microfluidic channels including CYTOP.

CYTOP (Poly[perfluoro(4-vinyloxy-1-butene)]) is a transparent fluoropolymer whose properties render it useful for a wide range of applications such as an insulator in organic semiconductors, a protective film coating, and a material for the fabrication of optical sensors [16]. CYTOP is chemically compatible with many organic solvents such as hexane, acetone, and isopropanol. Three types of CYTOP are available commercially, exploiting different terminal groups: M-grade with amide-silane terminal functional group (-CONH-Si(OR)$_n$), A-grade with carboxyl terminal functional group (-COOH), and S-grade with trifluoromethyl terminal group (-CF_3) as seen in Figure 5 [17].

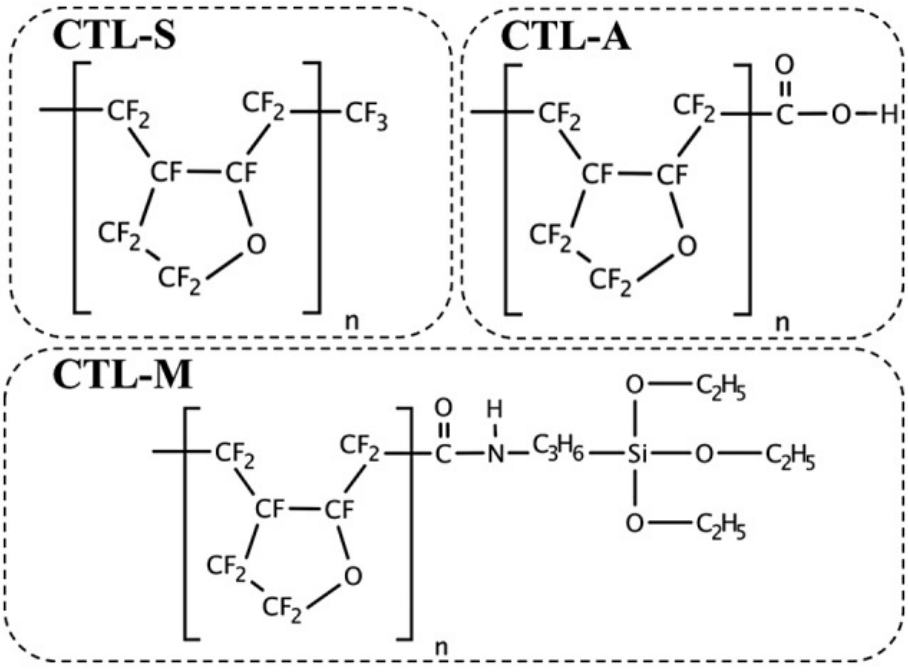

Figure 5. Chemical structures of the 3 grades of CYTOP: M, A and S. Adapted from [17].

While biosensing requires the specific binding of the analyte to the bioreceptor, proteins present in a fluid typically adsorb to any solid surface they come in contact with [18]. There are several factors that control the non-specific adsorption of proteins. External parameters under which experiments are conducted include temperature, pH, and ionic strength. Temperature influences both the equilibrium state and kinetics of protein adsorption, and generally higher temperatures result in increased adsorption rates. When the pH of the protein solution equals to the isoelectric point (pI) of a protein, the negative and positive charges are balanced resulting in a net neutral biomolecule. At a pH lower than pI, the protein is positively charged whereas at higher pH than pI, the protein is negatively charged. Charged proteins tend to greatly adsorb to substrates bearing an opposite charge. However, protein adsorption remains reportedly high when the electrostatic protein-protein repulsion is minimized at the pI (due to the net neutral charge of the protein) [18,19]. High ionic strength or the concentration of dissolved ions is responsible for shorter electrostatic interactions between charged entities which could explain the adsorption of charged proteins to like-charged substrates [18]. The protein size and its structural stability also have an influence on adsorption. Small proteins tend to diffuse quickly and adsorb more to material surfaces than bigger proteins. Proteins with lower thermodynamic stability adsorb more easily due to their easier unfolding than proteins with higher thermodynamic stability. When proteins unfold, more domains are revealed for further interaction with the surface.

Material surface properties, such as hydrophilicity/hydrophobicity, charge, topography, and chemical composition also play a role in adsorption. Generally, proteins adsorb to hydrophobic surfaces more than to hydrophilic ones. Water molecules compete with proteins to adsorb to a hydrophilic surface via the formation of hydrogen bonds, resulting in decreased protein adsorption and conformational change. On the contrary, when proteins interact with hydrophobic surfaces,

the ordered water layer is disturbed in an energetically favourable way, promoting protein adsorption. Increased roughness of material surfaces can also promote higher protein adsorption [18,19]. Understanding the chemical composition of the material surface is important in protein adsorption.

Of relevance to CYTOP for instance, functional groups of -CH3 have high affinity to fibrinogen (a protein involved in blood clotting), -OH groups have decreased affinity for plasma proteins, and -COOH groups have increased affinity for albumin [19]. Figure 6 shows infrared absorbance spectra of the CYTOP grades [17]. Electron affinity of CYTOP depends significantly on the terminal group; M-grade has the highest electron affinity followed by A-grade and S-grade [17]. Thus, when a negatively charged protein is in contact with CYTOP, it is more likely to stay adsorbed to the surface of M-grade, and least likely to stay adsorbed to S-grade.

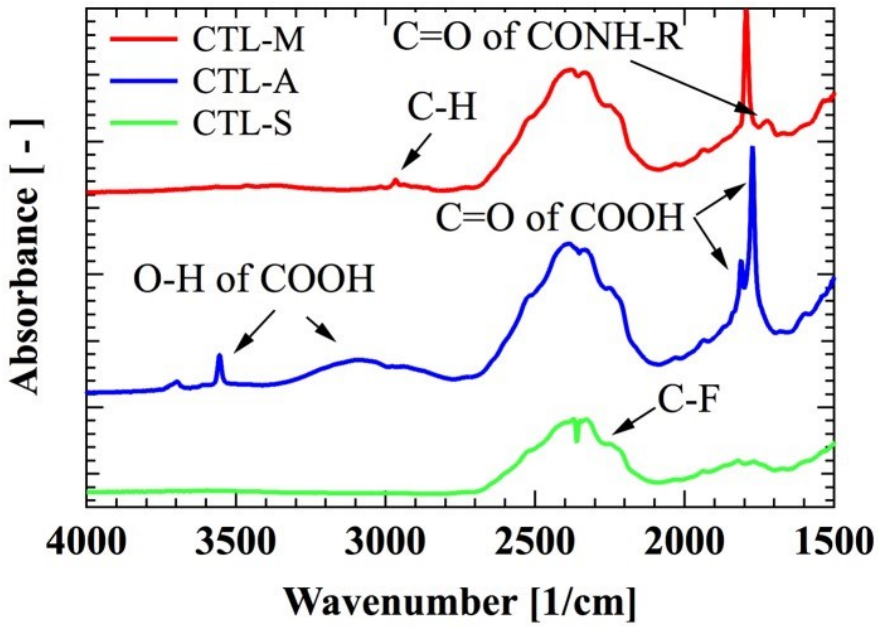

Figure 6. Infrared absorbance spectra of M-, A- and S-grade CYTOP. Adapted from [17].

1.5 Nanoantenna-based biosensors

Optical nanoantennas are similar to traditional radio-wave and microwave antennas that transmit and receive electromagnetic waves; however, they take the form of metallic nanostructures at optical (infrared and visible) wavelengths. Due to developments in nanofabrication, the realization of nanoantennas became feasible to demonstrate their potential to enhance the efficiency of sensing, light emission, photo-detection, spectroscopy, and heat transfer [20].

In Chapter 3, nanoantenna arrays are fabricated via helium ion beam lithography using a relatively thick single layer of poly(methyl methacrylate) (PMMA) as the resist to demonstrate pattern transfer through thermal evaporation and deposition of gold (thickness of up to 50 nm) and PMMA liftoff. A schematic diagram of the fabricated gold nanoantenna array on a fused silica substrate is depicted in Figure 7. This section provides an overview of nanoantenna-based biosensors.

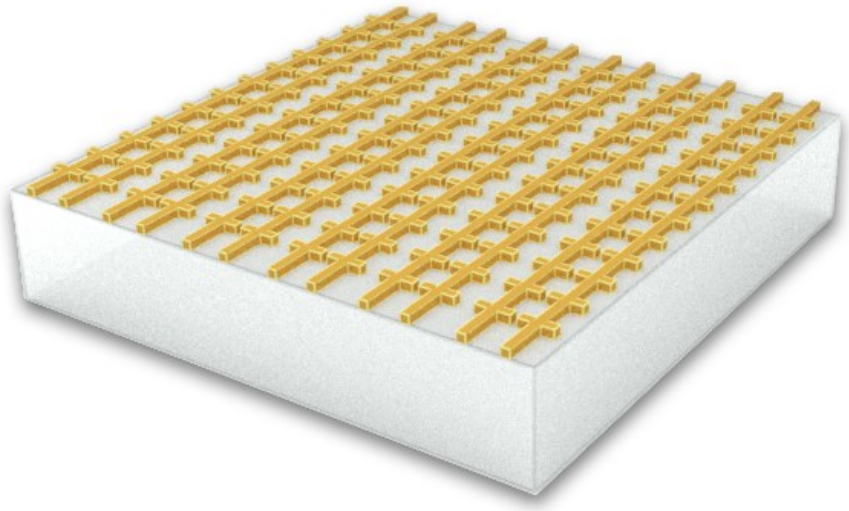

Figure 7. Schematic diagram of the fabricated gold nanoantenna array on a fused silica substrate

A similar geometry of the gold dipole nanoantennas fabricated in Chapter 3 has been assessed for bulk and surface biochemical sensing through finite-difference time domain (FDTD)

electromagnetic modelling [21]. These nanoantennas were assumed fabricated on a silicon substrate and covered with water. The array was excited through the back of the substrate offering a practical experimental setup as it separates the optics on the bottom of the substrate from the fluidics on top of the array. Observing the changes in wavelength at which the array resonates is a common way to measure changes in the refractive index of bulk solutions, and in the thickness or composition of the thin adlayer forming on the biosensor surface [21] (here the transducer is a nanoantenna array) due to biological interactions between the analyte and the bioreceptor. The local refractive index is changed from that of water to that of biomaterial post-binding (which is higher). From computed absorbance spectra of the array, it is noted that increasing the refractive index at the gold surface decreases the absorbance and red shifts the resonance wavelength. The bulk sensitivity (S_B) could be obtained from the following equation [22]:

$$S_B = \frac{\Delta\lambda_r}{\Delta n}$$

where $\Delta\lambda_r$ is the shift in surface plasmon resonance wavelength and Δn is the difference between the refractive index of the analyte adsorbed to the gold nanoantenna array and the refractive index of the bulk sensing solution (generally aqueous).

1.6 Thesis outline

This thesis includes two articles, both presently submitted for publication and under review. Chapter 2 discusses the non-specific adsorption of proteins to microfluidic material surfaces through measurement of the fluorescence intensity generated by labelled proteins adsorbed on the surface. The article outlines the fabrication process to form the surfaces, the microfluidic experiments conducted, the results of fluorescence intensity measurements in addition to surface characterization consisting of roughness and contact angle measurements. The article included in this chapter is in its "as submitted" format. Chapter 3 describes a new nanofabrication process to realise nano-antenna arrays and nanostructures on various substrates, including fused silica, Si, silver on Si, and MgO, using helium ion beam lithography and liftoff. The fabricated nanostructures were characterized using helium ion microscopy, atomic force microscopy, and were interrogated optically to obtain their transmittance response. This chapter includes an article in its "as submitted" format. Chapter 4 concludes this thesis and provides suggestions for future work. The thesis is then finalized with an appendix listing all chemicals used in Chapters 2 and 3, along with their hazards and storage requirements.

References

[1] N. Bhalla, P. Jolly, N. Formisano, P. Estrela, Introduction to biosensors, Essays Biochem. 60 (2016) 1–8. https://doi.org/10.1042/EBC20150001.

[2] D.W.G. Morrison, M.R. Dokmeci, U. Demirci, A. Khademhosseini, Clinical Applications of Micro- and Nanoscale Biosensors, Biomed. Nanostructures. (2007) 439–460. https://doi.org/doi:10.1002/9780470185834.ch17.

[3] C.R. Lowe, Overview of Biosensor and Bioarray Technologies, Handb. Biosens. Biochips. (2007). https://doi.org/doi:10.1002/9780470061565.hbb003.

[4] C. Karunakaran, R. Rajkumar, K. Bhargava, Chapter 1 - Introduction to Biosensors, in: C. Karunakaran, K. Bhargava, R.B.T.-B. and B. Benjamin (Eds.), Elsevier, 2015: pp. 1–68. https://doi.org/https://doi.org/10.1016/B978-0-12-803100-1.00001-3.

[5] D.R. Shankaran, K.V. Gobi, N. Miura, Recent advancements in surface plasmon resonance immunosensors for detection of small molecules of biomedical, food and environmental interest, Sensors Actuators B Chem. 121 (2007) 158–177. https://doi.org/https://doi.org/10.1016/j.snb.2006.09.014.

[6] H. Yu, Y. Peng, Y. Yang, Z.-Y. Li, Plasmon-enhanced light–matter interactions and applications, Npj Comput. Mater. 5 (2019) 45. https://doi.org/10.1038/s41524-019-0184-1.

[7] P. Berini, Long-range surface plasmon polaritons, Adv. Opt. Photonics. 1 (2009) 484–588. https://doi.org/10.1364/AOP.1.000484.

[8] O. Krupin, H. Asiri, C. Wang, R.N. Tait, P. Berini, Biosensing using straight long-range surface plasmon waveguides, Opt. Express. 21 (2013) 698–709. https://doi.org/10.1364/OE.21.000698.

[9] H. Asiri, Fabrication of surface plasmon biosensors in CYTOP, (2012).

[10] C. Chiu, E. Lisicka-Skrzek, R.N. Tait, P. Berini, Fabrication of surface plasmon waveguides and devices in Cytop with integrated microfluidic channels, J. Vac. Sci. Technol. B. 28 (2010) 729–735. https://doi.org/10.1116/1.3449187.

[11] O. Krupin, C. Wang, P. Berini, Selective capture of human red blood cells based on blood group using long-range surface plasmon waveguides, Biosens. Bioelectron. 53 (2014) 117–122. https://doi.org/https://doi.org/10.1016/j.bios.2013.09.051.

[12] O. Krupin, C. Wang, P. Berini, Detection of leukemia markers using long-range surface plasmon waveguides functionalized with Protein G, Lab Chip. 15 (2015) 4156–4165. https://doi.org/10.1039/C5LC00940E.

[13] W.R. Wong, S.D. Sekaran, F.R. Mahamd Adikan, P. Berini, Detection of dengue NS1 antigen using long-range surface plasmon waveguides, Biosens. Bioelectron. 78 (2016) 132–139. https://doi.org/10.1016/j.bios.2015.11.030.

[14] J.Y. Lichtenberg, Y. Ling, S. Kim, Non-Specific Adsorption Reduction Methods in Biosensing, Sensors (Basel). 19 (2019) 2488. https://doi.org/10.3390/s19112488.

[15] J.E. Contreras-Naranjo, O. Aguilar, Suppressing Non-Specific Binding of Proteins onto Electrode Surfaces in the Development of Electrochemical Immunosensors, Biosensors. 9 (2019) 15. https://doi.org/10.3390/bios9010015.

[16] AGC Inc. Chemicals Company-Cytop Technical Brochure. http://www.agc.com/kagaku/shinsei/cytop/en/.

[17] S. Kim, K. Suzuki, A. Sugie, H. Yoshida, M. Yoshida, Y. Suzuki, Effect of end group of amorphous perfluoro-polymer electrets on electron trapping, Sci. Technol. Adv. Mater. 19 (2018) 486–494. https://doi.org/10.1080/14686996.2018.1477395.

[18] M. Rabe, D. Verdes, S. Seeger, Understanding protein adsorption phenomena at solid surfaces, Adv. Colloid Interface Sci. 162 (2011) 87–106. https://doi.org/https://doi.org/10.1016/j.cis.2010.12.007.

[19] D.A. Puleo, R. Bizios, eds., Biological Interactions on Materials Surfaces Understanding and Controlling Protein, Cell, and Tissue Responses , 1st ed. 20, Springer New York, New York, NY, 2009. https://doi.org/10.1007/978-0-387-98161-1.

[20] L. Novotny, N. van Hulst, Antennas for light, Nat. Photonics. 5 (2011) 83–90. https://doi.org/10.1038/nphoton.2010.237.

[21] M. Alavirad, S.S. Mousavi, L. Roy, P. Berini, Schottky-contact plasmonic dipole rectenna concept for biosensing, Opt. Express. 21 (2013) 4328–4347. https://doi.org/10.1364/OE.21.004328.

[22] A. Abumazwed, W. Kubo, T. Tanaka, A.G. Kirk, Improved method for estimating adlayer thickness and bulk RI change for gold nanocrescent sensors, Sci. Rep. 8 (2018) 6683. https://doi.org/10.1038/s41598-018-24950-7.

Chapter 2 - Non-specific adsorption of protein to microfluidic materials

2.1. Summary

This chapter investigates the non-specific adsorption of fluorescently-labeled bovine serum albumin (BSA) by measuring the fluorescence intensity on multiple microfluidic materials: three grades of CYTOP (M-, A- and S-), silica, and SU-8. Sample fabrication process is described, along with the microfluidic experiments conducted to compare the non-specific adsorption (biofouling) occurring on each of the tested surfaces. A few surface properties relevant to protein adsorption are studied through the characterization of surface roughness with atomic force microscopy (AFM), and wettability via a water contact angle goniometer. The lowest adsorption occurred on SU-8, likely due to its hydrophilicity. Among the 3 grades of CYTOP considered, the lowest adsorption occurred on S-grade, which suggests its suitability in the implementation of optical biosensors in addition to its low refractive index.

2.2. Contribution

Sabaa Rashid fabricated the films, conducted the microfluidic experiments introducing a new experimental protocol, characterized the films in terms of their fluorescence, roughness, and wettability, and analyzed the results. Jesse Ward-Bond contributed to the experimental protocol. Oleksiy Krupin and Pierre Berini supervised the project. The manuscript was written by Sabaa Rashid and edited by Pierre Berini and Oleksiy Krupin.

2.3. Article

The following article is submitted for publication.

Non-specific adsorption of protein to microfluidic materials

Sabaa Rashid[a,d] Jesse Ward-Bond[a,d] Oleksiy Krupin,[b,d] Pierre Berini[b,c,d,*]

[a]Department of Chemical and Biological Engineering, University of Ottawa, Ontario, Canada
[b]School of Electrical Engineering and Computer Science, University of Ottawa, Ontario, Canada
[c]Department of Physics, University of Ottawa, Ontario, Canada
[d]Centre for Research in Photonics, University of Ottawa, Ontario, Canada

*Corresponding author: berini@eecs.uottawa.ca

Keywords: Non-specific adsorption, Biofouling, Biosensing, Surface characterization, CYTOP

Abstract

Non-specific adsorption of proteins to the surfaces of microfluidic channels poses a serious problem in lab-on-a-chip devices involving complex biological fluids. Materials commonly used in the formation of microfluidic channels include CYTOP, silica and SU-8. CYTOP is a transparent fluoropolymer with a low refractive index that approximately matches the refractive index of biologically compatible fluids, and is useful in optical biosensors. Using a microfluidic and fluorescence microscopy set-up, the non-specific adsorption of bovine serum albumin (BSA) labeled with fluorescein isothiocyanate (FITC) to three grades of CYTOP (S, M and A), silica, and SU-8 is investigated. Surface properties such as roughness and wettability are also characterized via an atomic force microscope and a contact angle measurement system. The non-specific adsorption of protein occurs with a highly variable load across these materials. Surprisingly, significantly lower adsorption occurred on SU-8 compared to the other materials, likely due to its hydrophilicity (post-cleaning). Among the 3 grades of CYTOP considered, the lowest adsorption occurred on S-grade. BSA adsorption to silica was higher than on S-grade CYTOP and

significantly higher than on SU-8 despite being hydrophilic, due to a fixed positive charge formed within the layer during fabrication, which attracts negatively-charged BSA in buffer.

1. Introduction

The non-specific adsorption (NSA) of protein to the surfaces of microfluidic channels is a serious problem in many lab-on-a-chip devices [1,2], particularly in affinity biosensors involving complex biological fluids (*e.g.*, blood products such as plasma and serum, mucous, nasopharyngeal fluid, urine, etc…) [3]. While biosensing requires specific adsorption of biomolecules to functionalized regions via immobilised bioreceptors such as antibodies or enzymes, proteins inevitably adsorb to un-functionalized regions of microfluidic chips resulting in biofouling. In addition to clogging channels, NSA may mask or falsify results in biosensing by reducing sensitivity and selectivity, by raising detection limits, or by causing cross-contamination between samples.

Minimising NSA in microfluidics depends in part on knowledge of the protein load that inherently forms on the material chosen to implement the channels and the underlying interaction mechanisms leading to the load. Non-specific protein affinity for a solid surface depends on the protein itself and its amino acid constituents which can be charged depending on the pH of their environment, as well as the size and structural stability of the protein [4]. The surface hydrophobicity, charge, topography, and chemical composition also significantly influence the NSA of proteins, in addition to the external conditions at which experiments are conducted [2,4].

Dielectric materials are commonly used in biosensor devices to implement microfluidic channels, or to introduce an insulating layer or an optical cladding in electronic, electrochemical or optical biosensors. Silica and SU-8 are often used for this purpose, and more recently, fluoropolymers. Understanding the NSA of proteins to such materials is fundamental to biosensor device applications.

SU-8 is composed of a polymeric epoxy resin, and a photoinitiator dissolved in cyclopentanone solvent, and used as a negative resist for defining structures in lithographic processes upon the exposure to UV light [5]. It has been used in many bioanalytical applications involving microfluidic channels and cell microculture systems [6], and exhibits poor adhesion of biomolecules to its surface [7].

CYTOP (Poly[perfluoro(4-vinyloxy-1-butene)]) is a transparent fluoropolymer whose properties render it useful for a wide range of applications such as an insulator in organic semiconductors, a protective film coating, and a material for the fabrication of optical fibers [8]. CYTOP is chemically compatible with many organic solvents such as hexane, acetone, and isopropanol. It has a low refractive index, similar to that of water [8], making it interesting for use in optical biosensors, including those based on surface plasmon resonance (SPR) which enable label-free real-time detection [9]. Three types of CYTOP are available commercially, exploiting different terminal groups: M-grade with amide-silane terminal functional group (-CONH-$Si(OR)_n$), A-grade with carboxyl terminal functional group (-COOH), and S-grade with trifluoromethyl terminal group ($-CF_3$) [8].

CYTOP has been used as a dielectric cladding and to form microfluidic channels in long-range surface plasmon-polariton (LRSPP)-based waveguide biosensors composed of a thin straight gold waveguide [10,11]. Once filled with the sensing fluid, the sensing channels become optically non-invasive because the refractive index of CYTOP is close to that of aqueous sensing solutions. The gold waveguide is functionalized with a self-assembled monolayer (SAM) bound to biological receptors (*e.g.*, antibodies) to later enable binding to the analyte (*e.g.*, antigen) when introducing a sensing fluid. This biosensor was used to demonstrate protein sensing using bovine serum

albumin (BSA) [12], the selective capture of human red blood cells [13], and the detection of leukemia markers using a functionalization strategy involving Protein G and antibodies [3].

Bovine Serum Albumin (BSA) is a globular protein that is commonly used to block non-specific interactions between cells and the underlying surface in cell adhesion research [14], or to block un-functionalised adsorption sites in biosensors when working with complex fluids [3]. Here we use BSA labelled with fluorescein isothiocyanate (FITC) as an NSA indicator, and investigate via fluorescence microscopy the BSA load on different surfaces, particularly, 3 grades of CYTOP (S, M, A), silica and SU-8. We also investigate the topography and wettability of the starting substrates using atomic force microscopy and contact angle microscopy.

2. Materials and methods

2.1 Sample fabrication

M-grade CYTOP (CTL-809M from AGC Chemicals Company) and A-grade CYTOP (CTX-809A from AGC Chemicals Company) were spin-coated on two p-type silicon wafers, 2-inch in diameter then the wafers were placed on a hot plate set to room temperature and ramped up to a temperature of 200 °C where the wafers were left for approximately 18 hours. A third 2-inch Si wafer was used to prepare S-grade CYTOP samples, by first spin-coating M-grade, then baking it at 50 °C for 30 minutes, then spin-coating S-grade CYTOP (CTX-809SP2 from AGC Chemicals Company) on top of the M-grade (S-grade CYTOP adheres poorly to a Si wafer). The wafer was then placed on a hot plate set to room temperature and ramped up to a temperature of 200 °C, then baked for approximately 18 hours.

SU-8 samples were prepared by spin-coating SU-8 2005 (formally MicroChem, now Kayaku Advanced Materials, Inc.) on another 2-inch Si wafer then subjecting it to a soft-bake of

65 °C for 5 minutes, followed by 10 minutes at 95 °C. The SU-8 film was then flood-exposed under UV light with an OAI 200IR mask aligner and an I-Line filter (365 nm bandpass) at 69 mJ/cm^2 exposure energy. Post-exposure, the wafer was then baked at 65 °C for 10 minutes, removed from the hot plate, and baked for another 20 minutes at 95 °C. Spin parameters of the 3 grades of CYTOP, along with SU-8 are shown in Table 1.

In addition to the aforementioned films, a 2-inch Si wafer bearing a 100 nm thick layer of thermally grown silica (gate oxide - dense amorphous SiO_2, Carleton University, Ottawa, Canada) was used.

The thicknesses of M-, A- and S-grade CYTOP and SU-8 films were measured to be 1.65, 2.3, 2.5, and 0.68 μm, respectively. CYTOP, silica and SU-8 have refractive indices of about 1.34 [8], 1.46 [15], and 1.59 [16], respectively.

Table 1. CYTOP grades and SU-8 spin parameters on Laurell WS-650-23NPP spin coater

Substance	Step	Spin Speed (rpm)	Acceleration (rpm/s)	Duration (s)
M-grade CYTOP	1	500	200	3
	2	500	0	10
	3	1000	200	3
	4	1000	0	30
	5	0	-200	6
A-grade CYTOP and S-grade CYTOP	1	1000	200	6
	2	1000	0	10
	3	1500	200	3
	4	1500	0	30
	5	0	-300	5
SU-8 2005	1	1000	200	6
	2	1000	0	10
	3	4000	600	6
	4	4000	0	30
	5	0	-700	6

2.2 Solution preparation

Fluorescein isothiocyanate (FITC) labeled bovine serum albumin (BSA) and phosphate buffer saline (PBS) 0.01 M, pH 7.4 were obtained from Sigma-Aldrich. PBS solution was prepared from the package by dissolving it in 1 L of deionized water producing a buffer of the following constitution: 0.01 M phosphate buffer saline, 0.138 M NaCl and 0.0027 M KCl (according to the manufacturer). BSA solution was prepared by mixing the FITC-labeled BSA with PBS to a concentration of 100 μg mL^{-1}.

2.2 Experimental

A custom fluidic jig was used to conduct NSA experiments, composed of a Plexiglas lid with two holes for the inlet and outlet microfluidic tubings, a fluorocarbon O-Ring (Apple Rubber Products Inc.) attached to the bottom of the lid facilitating an effective seal and fluid exchange, and a metal base (Al) to support the chip in a groove and the lid with screws, as shown in Fig. 1.

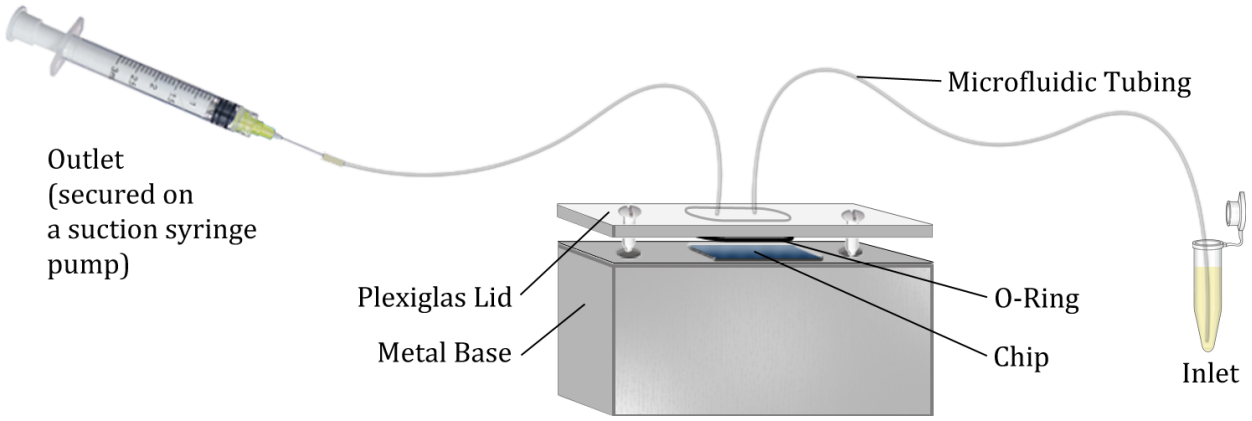

Fig. 1. Schematic diagram of the fluidic jig used for conducting the non-specific adsorption of BSA to different thin films with integrated microfluidic tubings having an outer diameter of 550 μm and inner diameter of 250 μm (IDEX). The BSA and PBS solutions flow from right to left.

The wafers (See sub-section 2.1 *Sample fabrication*) were cleaved using a diamond-tipped pen into approximately 6 × 5 mm^2 chips to fit in the groove of the metal base of the custom fluidic

jig shown in Fig. 1. The wafers were cleaved rather than diced to avoid re-depositing debris formed while dicing, thus decreasing contamination and surface particulate. The cleaved chips were then washed with distilled/deionized water (DDIH_2O), followed by isopropanol (IPA) wash, dried with nitrogen gas, and placed into a UV/Ozone chamber (Novascan, PSD-UV4) for 15 minutes with the UV lamp on and an additional 15 minutes with the UV lamp off to remove any possible organic surface contaminants.

A chip was then placed and secured on the metal base of the fluidic jig (Fig. 1). To prepare the chip and fluidic tubing, IPA in a syringe was manually injected, forming a pressure-driven flow from left to right in the microfluidic channel (Fig. 1), followed by injection of DDI water using a second syringe, and a final injection of PBS using a third syringe. Priming with IPA first was necessary to prevent the trapping of air bubbles since IPA wets the chip and tubing more effectively than water.

The PBS syringe was then secured to a Pico Plus syringe pump (from Harvard Apparatus), set to operate under suction, such that fluids would now be pulled through the microfluidic channel from right to left (Fig. 1), and the PBS syringe used to receive waste. BSA solution in a vial was used as the input fluid and the pump was set to run for 14 minutes at a flowrate of 30 μL min^{-1}, ensuring complete exchange of fluid in the microfluidic channel and full exposure of its inner surfaces to BSA. The pump was stopped and the pressure was allowed to stabilize in the system before replacing the BSA vial with a vial containing PBS only, in order to rinse the chip and remove any non-adsorbed BSA, by running for 14 minutes at the same flowrate. The chip was subsequently placed on a microscope slide, covered with a droplet of VectaShield anti-fade mounting medium (Vector Laboratories, H-1000-10), and sealed with a coverslip on top.

The experiment was repeated 3 times on different chips (set 1) for each tested surface. Another set of 3 chips (set 2) was placed on a microscope slide immediately after the UV/Ozone treatment, covered with the anti-fade mounting medium and a coverslip to produce negative-control chips that were not exposed to the BSA solution. The 2 sets of samples were stored in the refrigerator, protected from light, at 4 °C until inspected via fluorescence microscopy.

In Addition, several chips from the same wafers were used for roughness measurement with atomic force microscopy (AFM), and water contact angle measurements shortly after the UV/Ozone exposure.

2.4 Characterization

Fluorescence Microscopy: The NSA of FITC-labeled BSA to 3 grades of CYTOP, silica and SU-8 was evaluated through the use of a Nikon Ni-U upright ratiometric fluorescence microscope, using a Nikon Plan Apo objective lens with a magnification of 10× and a numerical aperture of 0.45. Fluorescence images were captured using an Andor iXon Ultra 897 cooled EMCCD camera. The chips were illuminated using a laser source of wavelength λ_0 = 475 nm (spectraX), and FITC fluorescence was isolated using 512/45 emission filter (489.5-534.5 nm). The average fluorescence intensity over areas of 819 × 819 μm^2 was calculated as the average of 16-bit pixel intensity values, using NIS-Elements AR software and MATLAB. Three chips that were exposed to BSA were visualized near their centre, and 3 other negative-control chips were visualized at several locations (3 measurements per chip) to account for auto-fluorescence on the negative-control chips.

Atomic Force Microscopy (AFM): Non-contact-mode AFM roughness images of the chips were obtained using a Park Systems NX10 AFM with a Tap300Al-G tip from NanoAndMore.

Contact Angle Measurements: Static water contact angle was measured with a VCA Optima System (AST Products Inc.). A 1 μL droplet of DI water was dispensed onto a chip using an integrated micro-syringe. The contact angle was calculated based on placing manual markers surrounding the droplet. Nine measurements were averaged per tested surface. Images of the DI water droplet on the films (found in Table. 2) were captured using the camera of the VCA Optima System.

3. Results and discussion

Fluorescence microscopy was used to test the non-specific adsorption of BSA labeled with FITC to 3 grades of CYTOP, silica and SU-8. The averaged intensity was calculated over 3 chips of each film, corrected by subtracting the averaged intensity calculated over 9 measurements on negative-control samples not exposed to BSA (to account for auto-fluorescence), yielding the relative fluorescence intensity plotted in Fig. 2. It is worth noting that SU-8 produced the highest auto-fluorescence intensity of all negative-control chips, an observation that is consistent with the strong auto-fluorescence reported in the literature for this material [17]. The variance of positive intensities var(P) was added to the variance of the negative-control intensities var(N) to find the standard deviation (σ) as shown in Eq. 1, and represented by the error bars on Fig. 2.

$$\sigma = \sqrt{var(P) + var(N)} \qquad (1)$$

The results given in Fig. 2 show that the highest amount of BSA was adsorbed to M-grade CYTOP and the least to S-grade CYTOP among the 3 CYTOP grades. Adsorption to the silica surface was between those observed for A-grade and S-grade CYTOP. Adsorption to SU-8 was significantly lower than for all other substrates. Notably, the small error bars were achieved by optimising the experimental protocol to that described in Section 2.2 (*i.e.*, introducing the buffer

solution prior to introducing the BSA solution after priming with IPA and DI water), in addition to minimising the surface roughness through careful process control, minimising debris and contamination by cleaving the wafers into chips rather than dicing, and applying appropriate cleaning steps before commencing the experiments.

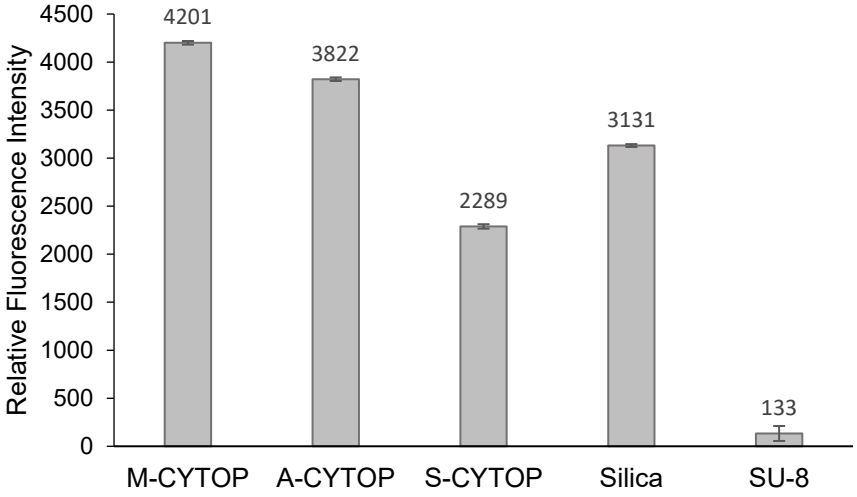

Fig. 2. Comparison of FITC-labeled-BSA adsorption to 3 grades of CYTOP, silica and SU-8 after exposing the surfaces to 100 μg mL^{-1} of fluorescently-labeled BSA by measuring the fluorescence intensity. The data of each bar corresponds to the relative fluorescence intensity, ±1 standard deviation calculated from 3 positive independent experiments and 9 negative-control measurements.

To further investigate the results shown in Fig. 2, the surface roughness and wettability were evaluated using an AFM and a contact angle measurement system. Fig. 3(a) reveals sub-1 nm average surface roughness (R_a) values for all films, taken over areas of 20 × 20 μm^2. R_a is low and similar for all films, suggesting that roughness does not play a significant role in the NSA of BSA to the films.

Fig. 3(b) shows the averaged water contact angle measured on each film. The 3 CYTOP grades are hydrophobic since their contact angle is above 90°, whereas silica and SU-8 are hydrophilic since their contact angle is below 90°. SU-8 typically has a water contact angle of

approximately 78° [6], which differs significantly from the one measured here (52° ± 2°) due to treatment with UV/Ozone and the formation of hydrophilic functional groups on the SU-8 surface. A higher BSA load was observed for the hydrophobic films (particularly M- and A-grade CYTOP). This is likely due to the energetically-preferred interaction of ordered water molecules with each other in solution, rather than competing with BSA to adsorb to the hydrophobic film [4]. When protein interacts with the film, the ordered water layer is disturbed in an energetically favourable way, encouraging protein adsorption. S-grade CYTOP exhibited lower adsorption of BSA likely due to its -CF_3 terminal group which limits protein adsorption [18], compared to the amide-silane functional groups in M-grade CYTOP that form strong covalent bonds, and carboxyl functional groups in A-grade CYTOP that form hydrogen bonds [19] upon interaction with proteins. This is also consistent with the charge-trapping characteristics of the 3 grades of CYTOP which strongly depend on their terminal group. The order of solid-state electron affinity was found to be S-grade < A-grade < M-grade [20]. Significantly lower BSA was adsorbed to SU-8, possibly due the hydrophilicity of the film on which water molecules compete with protein through the formation of hydrogen bonds. However, this explanation does not apply to the silica film despite its hydrophilicity. Rather, the thermal growth of silica on silicon produces positive trapped charge in the layer [21], resulting in the attraction of protein if the latter is negatively charged, as is the case here with BSA in a buffer at a pH of 7.4 (the isoelectric point of BSA is ~ 4.7) [22].

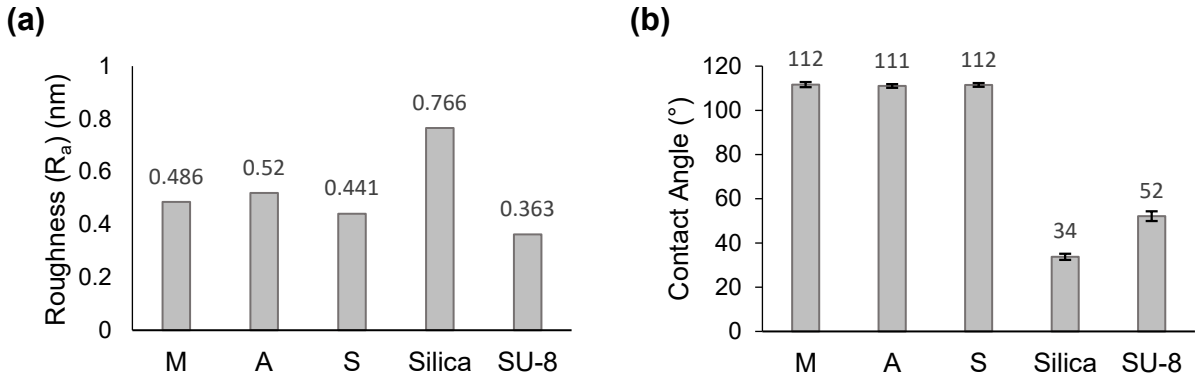

Fig. 3. (a) Sub-1 nm averaged surface roughness (R_a) over an area of 20 × 20 μm^2 measured with an AFM on the M-grade CYTOP, A-grade CYTOP, S-grade CYTOP, silica, and SU-8 films. (b) Water contact angle measured on the same 3 CYTOP grades, silica, and SU-8 films. Measurements show that all CYTOP grades are hydrophobic since their contact angle is above 90°, contrary to silica and SU-8 which are hydrophilic because their contact angle is below 90°.

Table 2 summarises the results discussed in this section. The second column gives typical fluorescence images taken over an 819 × 819 μm^2 area of FITC-labeled-BSA adsorbed on surfaces of each of the 3 CYTOP grades, silica and SU-8. The next column gives typical AFM scans taken over a 20 × 20 μm^2 area on each tested surface and over which the averaged surface roughness (R_a) was measured. The last column gives example images of a water droplet on each film used in calculating the averaged contact angle.

Table 2. Summary of the characterization results of each film: Typical fluorescence images obtained over an area of 819 × 819 μm^2, typical AFM scans taken over an area of 20 × 20 μm^2, and water droplet images used for measuring the static contact angle.

Film	Fluorescence Image	AFM Scan	Water Droplet
M-CYTOP	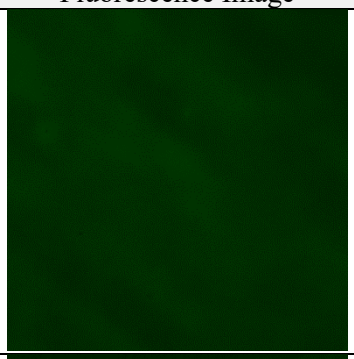	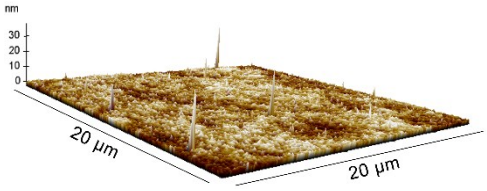	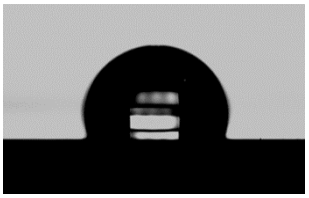
A-CYTOP		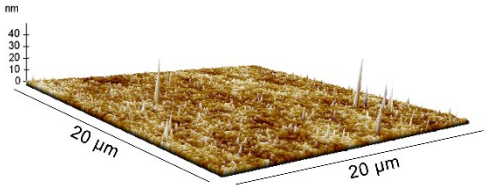	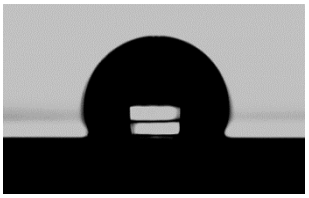
S-CYTOP	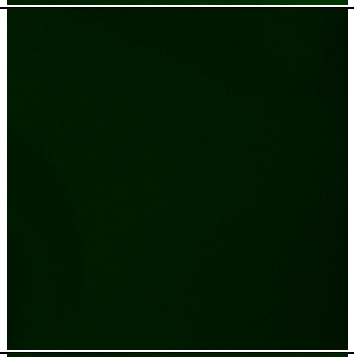	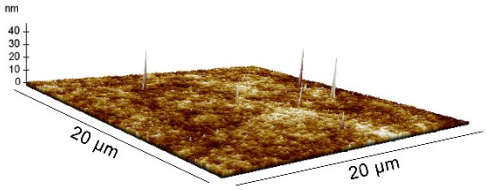	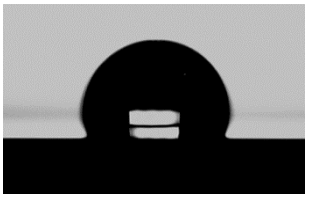
Silica	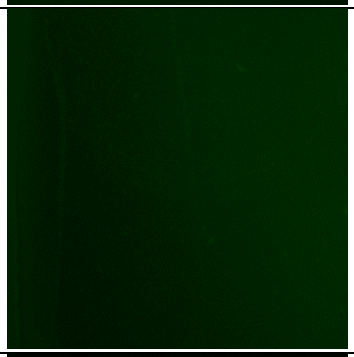	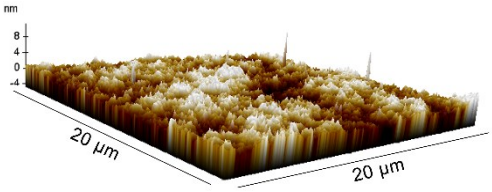	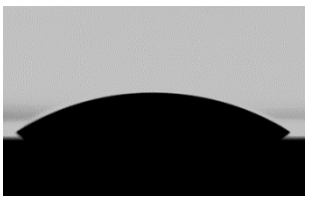
SU-8	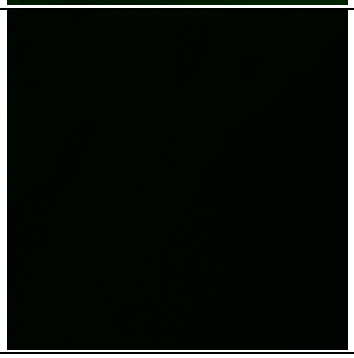	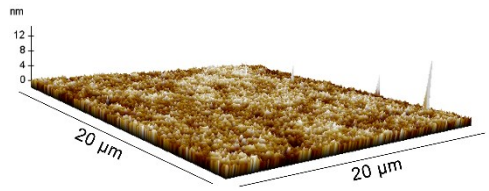	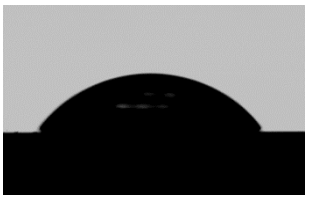

4. Summary and conclusions

The non-specific adsorption of 100 μgmL^{-1} BSA in PBS to CYTOP (A-, S-, and M-grade), silica and SU-8 films on silicon was investigated through measurements of fluorescence intensity of BSA labeled with FITC. Surface roughness and water contact angle measurements on all films were measured to support the analysis. All surfaces were cleaned using IPA and DI water, then subjected to a UV-Ozone treatment immediately before exposure to the BSA solution. The lowest adsorption occurred on SU-8, likely due to its hydrophilicity. Among the 3 grades of CYTOP considered, the lowest adsorption occurred on S-grade. BSA adsorption to silica was higher than on S-grade CYTOP and SU-8 despite being hydrophilic, due to fixed positive charge trapped in thermally grown silica on silicon and BSA being negatively charged in pH neutral buffer.

Acknowledgments

Financial support provided by the Natural Sciences and Engineering Research Council (NSERC) of Canada is gratefully acknowledged. Anthony Olivieri and Howard Northfield are gratefully acknowledged for their assistance. R. Niall Tait and Rob Vandusen are gratefully acknowledged for supplying thermally-grown silica film on silicon wafers.

References

[1] J.Y. Lichtenberg, Y. Ling, S. Kim, Non-Specific Adsorption Reduction Methods in Biosensing, Sensors (Basel). 19 (2019) 2488. https://doi.org/10.3390/s19112488.

[2] M. Rabe, D. Verdes, S. Seeger, Understanding protein adsorption phenomena at solid surfaces, Adv. Colloid Interface Sci. 162 (2011) 87–106. https://doi.org/https://doi.org/10.1016/j.cis.2010.12.007.

[3] O. Krupin, C. Wang, P. Berini, Detection of leukemia markers using long-range surface plasmon waveguides functionalized with Protein G, Lab Chip. 15 (2015) 4156–4165. https://doi.org/10.1039/C5LC00940E.

[4] D.A. Puleo, R. Bizios, eds., Biological Interactions on Materials Surfaces Understanding and Controlling Protein, Cell, and Tissue Responses , 1st ed. 20, Springer New York, New

York, NY, 2009. https://doi.org/10.1007/978-0-387-98161-1.

[5] F. Ceyssens, R. Puers, SU-8 Photoresist BT - Encyclopedia of Nanotechnology, in: B. Bhushan (Ed.), Springer Netherlands, Dordrecht, 2012: pp. 2530–2543. https://doi.org/10.1007/978-90-481-9751-4_360.

[6] C.-J. Chang, C.-S. Yang, L.-H. Lan, P.-C. Wang, F.-G. Tseng, Fabrication of a SU-8-based polymer-enclosed channel with a penetrating UV/ozone-modified interior surface for electrokinetic separation of proteins, J. Micromechanics Microengineering. 20 (2010) 115031. https://doi.org/10.1088/0960-1317/20/11/115031.

[7] Y. Wang, J.-H. Pai, H.-H. Lai, C.E. Sims, M. Bachman, G.P. Li, N.L. Allbritton, Surface graft polymerization of SU-8 for bio-MEMS applications, J. Micromechanics Microengineering. 17 (2007) 1371–1380. https://doi.org/10.1088/0960-1317/17/7/020.

[8] AGC Inc. Chemicals Company-Cytop Technical Brochure. http://www.agc.com/kagaku/shinsei/cytop/en/.

[9] D.R. Shankaran, K.V. Gobi, N. Miura, Recent advancements in surface plasmon resonance immunosensors for detection of small molecules of biomedical, food and environmental interest, Sensors Actuators B Chem. 121 (2007) 158–177. https://doi.org/https://doi.org/10.1016/j.snb.2006.09.014.

[10] C. Chiu, E. Lisicka-Skrzek, R.N. Tait, P. Berini, Fabrication of surface plasmon waveguides and devices in Cytop with integrated microfluidic channels, J. Vac. Sci. Technol. B. 28 (2010) 729–735. https://doi.org/10.1116/1.3449187.

[11] P. Berini, Long-range surface plasmon polaritons, Adv. Opt. Photonics. 1 (2009) 484–588. https://doi.org/10.1364/AOP.1.000484.

[12] O. Krupin, H. Asiri, C. Wang, R.N. Tait, P. Berini, Biosensing using straight long-range surface plasmon waveguides, Opt. Express. 21 (2013) 698–709. https://doi.org/10.1364/OE.21.000698.

[13] O. Krupin, C. Wang, P. Berini, Selective capture of human red blood cells based on blood group using long-range surface plasmon waveguides, Biosens. Bioelectron. 53 (2014) 117–122. https://doi.org/https://doi.org/10.1016/j.bios.2013.09.051.

[14] P.A. Dimilla, S.M. Albelda, J.A. Quinn, Adsorption and elution of extracellular matrix proteins on non-tissue culture polystyrene petri dishes, J. Colloid Interface Sci. 153 (1992) 212–225. https://doi.org/https://doi.org/10.1016/0021-9797(92)90313-B.

[15] W.A. Pliskin, R.P. Esch, Refractive Index of SiO2 Films Grown on Silicon, J. Appl. Phys. 36 (1965) 2011–2013. https://doi.org/10.1063/1.1714393.

[16] A. Borreman, A.M.S. Musa, A. Kok, M.B.J. Diemeer, A. Driessen, Fabrication of Polymeric Multimode Waveguides and Devices in SU-8 Photoresist Using Selective Polymerization, in: IEEE/LEOS Benelux Chapter Annu. Symp. 2002, Vrije Universiteit Amsterdam, Amsterdam, 2002: pp. 83–86. http://doc.utwente.nl/58192/.

[17] J.-H. Pai, Y. Wang, G.T. Salazar, C.E. Sims, M. Bachman, G.P. Li, N.L. Allbritton, Photoresist with low fluorescence for bioanalytical applications, Anal. Chem. 79 (2007)

8774–8780. https://doi.org/10.1021/ac071528q.

[18] G. Altankov, K. Richau, T. Groth, The role of surface zeta potential and substratum chemistry for regulation of dermal fibroblasts interaction, Materwiss. Werksttech. 34 (2003) 1120–1128. https://doi.org/10.1002/mawe.200300699.

[19] Y. Sakane, Y. Suzuki, N. Kasagi, The development of a high-performance perfluorinated polymer electret and its application to micro power generation, J. Micromechanics Microengineering. 18 (2008) 104011. https://doi.org/10.1088/0960-1317/18/10/104011.

[20] S. Kim, K. Suzuki, A. Sugie, H. Yoshida, M. Yoshida, Y. Suzuki, Effect of end group of amorphous perfluoro-polymer electrets on electron trapping, Sci. Technol. Adv. Mater. 19 (2018) 486–494. https://doi.org/10.1080/14686996.2018.1477395.

[21] D.R. Lamb, Some electrical properties of the silicon-silicon dioxide system, Thin Solid Films. 5 (1970) 247–276. https://doi.org/https://doi.org/10.1016/0040-6090(70)90096-9.

[22] L. Medda, M. Monduzzi, A. Salis, The molecular motion of bovine serum albumin under physiological conditions is ion specific, Chem. Commun. (Camb). 51 (2015) 6663–6666. https://doi.org/10.1039/C5CC01538C.

Chapter 3 - Nanofabrication by helium ion beam

3.1. Helium ion beam lithography and liftoff: A new nanofabrication process

3.1.1. Summary

This section describes a novel nanofabrication process using the helium ion microscope (HIM), exploiting negligible proximity effects and higher resist sensitivity when compared to an electron beam. The process is similar to a conventional electron beam lithography and liftoff process, in which a radiation-sensitive material is exposed, developed, metallized and lifted-off. Isolated gold lines, 20 nm thick and as narrow as 14 nm have been fabricated, along with 50% duty cycle gratings of 60 nm pitch. A manual overlay alignment process is also demonstrated to establish electrical nanoscale connections to pre-existing fan-out microstructures (our HIM instrument is not equipped with a precision translation stage - *e.g.*, controlled via laser interferometry - or the beam control system required to allow write-field stitching and automated overlay alignment). Nanoantenna arrays have been successfully fabricated and characterised through HIM and atomic force microscopy (AFM) which show a high degree of agreement with the target layout dimensions. In addition, the fabrication of these arrays has been validated by interrogating the arrays optically in terms of their transmittance response, and comparing the measurements to the theoretical transmittance response which was calculated numerically via 3D finite-difference time-domain (FDTD) electromagnetic simulations.

3.1.2. Contribution

Sabaa Rashid developed the helium ion beam lithography and liftoff process, carried out the nanofabrication work including electron beam exposures to reveal the alignment marks needed for the manual overlay alignment. She analyzed the Raman scattering measurements and characterised

the fabricated nanostructures via AFM and HIM. Jaspreet Walia performed the Raman scattering measurements. Howard Northfield carried out the optical lithography and liftoff work required to fabricate the fan-out microstructures. Choloong Hahn and Anthony Olivieri built the optical setup and performed the transmittance response measurements. Antonio Calà Lesina performed the 3D-FDTD simulations for the theoretical transmittance response. Fabio Variola enabled the Raman scattering measurements. Arnaud Weck, Lora Ramunno and Pierre Berini supervised the project. The manuscript was written by Sabaa Rashid, except for the description of the FDTD simulations which was written by Antonio Calà Lesina. The manuscript was edited by Pierre Berini.

3.1.3. Article

The following article is submitted for publication.

Helium ion beam lithography and liftoff

Sabaa Rashid,[a,b] Jaspreet Walia,[b,c] Howard Northfield,[b] Choloong Hahn,[b,c] Anthony Olivieri,[b] Antonio Calà Lesina,[d,e,f] Fabio Variola,[g] Arnaud Weck,[b,g,h] Lora Ramunno,[b,h] and Pierre Berini [b,c,h,*]

[a]Department of Chemical and Biological Engineering, University of Ottawa, 161 Louis Pasteur, Ottawa, Ontario K1N 6N5, Canada.
[b]Centre for Research in Photonics, University of Ottawa, 25 Templeton Street, Ottawa, Ontario K1N 6N5, Canada.
[c]School of Electrical Engineering and Computer Science, University of Ottawa, 800 King Edward Avenue, Ottawa, Ontario K1N 6N5, Canada.
[d]Hannover Centre for Optical Technologies, Leibniz Universität Hannover, Hannover, Germany
[e]Cluster of Excellence PhoenixD (Photonics, Optics, and Engineering – Innovation Across Disciplines), Hannover, Germany
[f]Institut für Transport- und Automatisierungstechnik, Fakultät für Maschinenbau, Leibniz Universität Hannover, Hannover, Germany
[g]Department of Mechanical Engineering, University of Ottawa, 161 Louis Pasteur, Ottawa, Ontario K1N 6N5, Canada.
[h]Department of Physics, University of Ottawa, 150 Louis Pasteur, Ottawa, Ontario K1N 6N5, Canada.

*Corresponding author: berini@eecs.uottawa.ca

Abstract

We introduce a Helium Ion Beam Lithography (HIBL) and liftoff process that can be used for the fabrication of arbitrary nanostructures. The process offers several advantages: it exploits high-resolution positive tone resists commonly used in electron-beam lithography, such as poly (methyl methacrylate) (PMMA). The exposing helium ion beam produces a high secondary electron yield, leading to high resist sensitivity and fast patterning speeds. Proximity effects are negligible due to the low count of backscattered helium ions from the substrate through the resist layer causing unwanted exposure. The process is transferrable with minimal alteration among conductive or insulating substrates, such as doped silicon, metal-coated silicon, fused silica and magnesium oxide. The process can be used to pattern any material compatible with liftoff, such as evaporated

metals or dielectrics. The process is demonstrated for several PMMA thicknesses with a view towards lifting off materials of different thicknesses. Isolated lines as narrow as 14 nm, and line-space gratings of 40 nm pitch (50% duty cycle), are produced as resolution tests by lifting off an evaporated 20 nm thick Au film. Plasmonic nanoantenna arrays are also produced as demonstration structures, for which optical measurements are in excellent agreement with simulations. Lithographic overlay has also been developed to precision-align nanostructures to microstructures realised beforehand on the substrate via UV lithography. The process is useful for the rapid patterning of nanostructures in general.

Introduction

Nanofabrication techniques are of a great interest due to the exploitation of unique properties that emerge when devices and systems are miniaturised. Nanofabrication allows advancements in photonics such as the realization of metasurfaces or nanoantenna arrays in applications such as biosensing and beam steering.[1,2] One of most prevalent nano-patterning techniques available is electron beam lithography (EBL) where an electron sensitive resist is exposed and developed. The generated pattern in the resist is subsequently transferred to another layer through an etching or liftoff process. However, electron beam lithography suffers from proximity effects that limit the patterning resolution at the nanoscale.[3] A potential alternative nano-patterning technique is helium ion beam lithography (HIBL).[4] HIBL using PMMA (poly (methyl methacrylate)) was first demonstrated by generating lines with a resolution of about 200 nm using an in-house constructed helium field ion source.[5]

Carl Zeiss SMT Inc. commercially released the Orion NanoFab helium ion microscope (HIM), based on the gas field ion source technology, which allows an imaging resolution of 0.5

nm.[6,7] Since its introduction, the HIM has been used in high-resolution imaging of biological and insulating samples by utilizing an integrated electron flood gun that locally neutralises the positive charge deposited by the helium ions scanning the sample.[7,8] It has also been used in nanoscale fabrication by direct milling.[3,9]

The helium ion beam in a HIM can be focused to a spot size as low as 0.25 nm due to its small de Brogile wavelength, and the atomically sharp tungsten tip used to ionize helium atoms (the tip consists of a 3-atom tungsten trimer). Consequently, the convergence angle in a HIM is smaller than a scanning electron microscope, resulting in less diffraction effects and a longer depth of field.[6,8] Contrary to EBL, proximity effects are negligible in HIBL due to the significantly lower count of backscattered ions from the substrate through the resist layer causing unwanted exposure. Furthermore, a helium ion beam generates a higher secondary electron yield than an electron beam of comparable energy, which leads to higher resist sensitivity and faster patterning speeds.[3,5,10,11]

Work on HIBL has been limited to patterning thin layers of various resists, particularly negative tone resists.[4,5,10-20] Patterning of 6 nm diameter dots in 5 nm thick hydrogen silsesquioxane (HSQ),[12] 10 nm wide lines arranged in a 20 nm pitch in 25 nm thick HSQ,[10] 12 nm wide lines in 20 nm thick PMMA,[13] 9 nm wide lines arranged in a 17 nm pitch in 10 nm thick negative fullerene-based resist,[14] 9 nm wide lines in 21 nm thick negative hafnium oxide peroxide hydroxide sulfate (HafSOx) resist,[15] 5 nm wide lines in 20 nm thick alumina based resist,[16] 9 nm wide isolated lines in 30 nm thick nickel-based negative tone metal oxide cluster resist (Ni-MOC).[17] High density gratings of 35 nm pitch patterned in 30 nm-thick HSQ over a large area ($100 \times 100\ \mu m^2$) have also been patterned in addition to patterning on tilted surfaces.[18] Recently, 5 nm wide lines arranged in a 16 nm pitch, transferred into silicon through dry etching using a 3.5 nm thick metal-organic negative tone resist as an etch mask, have been reported.[19] Notably, the

narrowest nanowires fabricated using EBL and liftoff are formed of 10 nm thick titanium, 14 ± 2 nm wide, separated by 28 nm.[20]

As surveyed above, all research thus far on HIBL has been oriented toward patterning thin layers of various resists, particularly negative tone resists. In this paper, pattern transfer via liftoff of a single-layer PMMA mask exposed using HIBL is proposed and demonstrated. Specifically, a PMMA mask is applied, then exposed, developed, metallised, and lifted off to realise nanoscale metallic structures, such as arrays of electrically-contacted nanoantennas, isolated lines, and line-space gratings. Different PMMA thicknesses are considered with a view toward lifting off different thicknesses of deposited material. Insulating and conductive substrates were also used.

Nanofabrication process

Target nanostructures

The gold nanoantenna array of interest is sketched in the last panel of Figure 1A, and a sketch of the unit cell is shown in Figure 1B along with the target dimensions. The unit cell, of dimensions 500×227 nm^2, is replicated in the plane to form a 10×10 μm^2 array. The array is formed on a fused silica substrate. The dimensions and materials were selected such that the fundamental plasmonic resonance of the system would appear in the wavelength range $\lambda_0 = 800$ to 1000 nm (for ease of testing). Perpendicular gold contacts establish electrical connections to each arm of the dipoles. Such contacts were included in the design because they are challenging to fabricate at the nanoscale, and contacts anticipate application of the nanoantenna arrays to optoelectronic biosensing[1] or beam steering.[2] Nanoantenna arrays aligned and connected to fan-out microstructures defined beforehand using UV lithography and liftoff were also included to motivate development of HIBL overlay alignment techniques.

In addition to contacted nanoantenna arrays, line-space gratings of duty cycle 50%, pitch 20, 40, 60, 80 and 100 nm, and length 5 μm were also fabricated, as were arrays of isolated single-pixel lines, 10 μm in length, separated by 100 nm, in order to determine the resolution of the process.

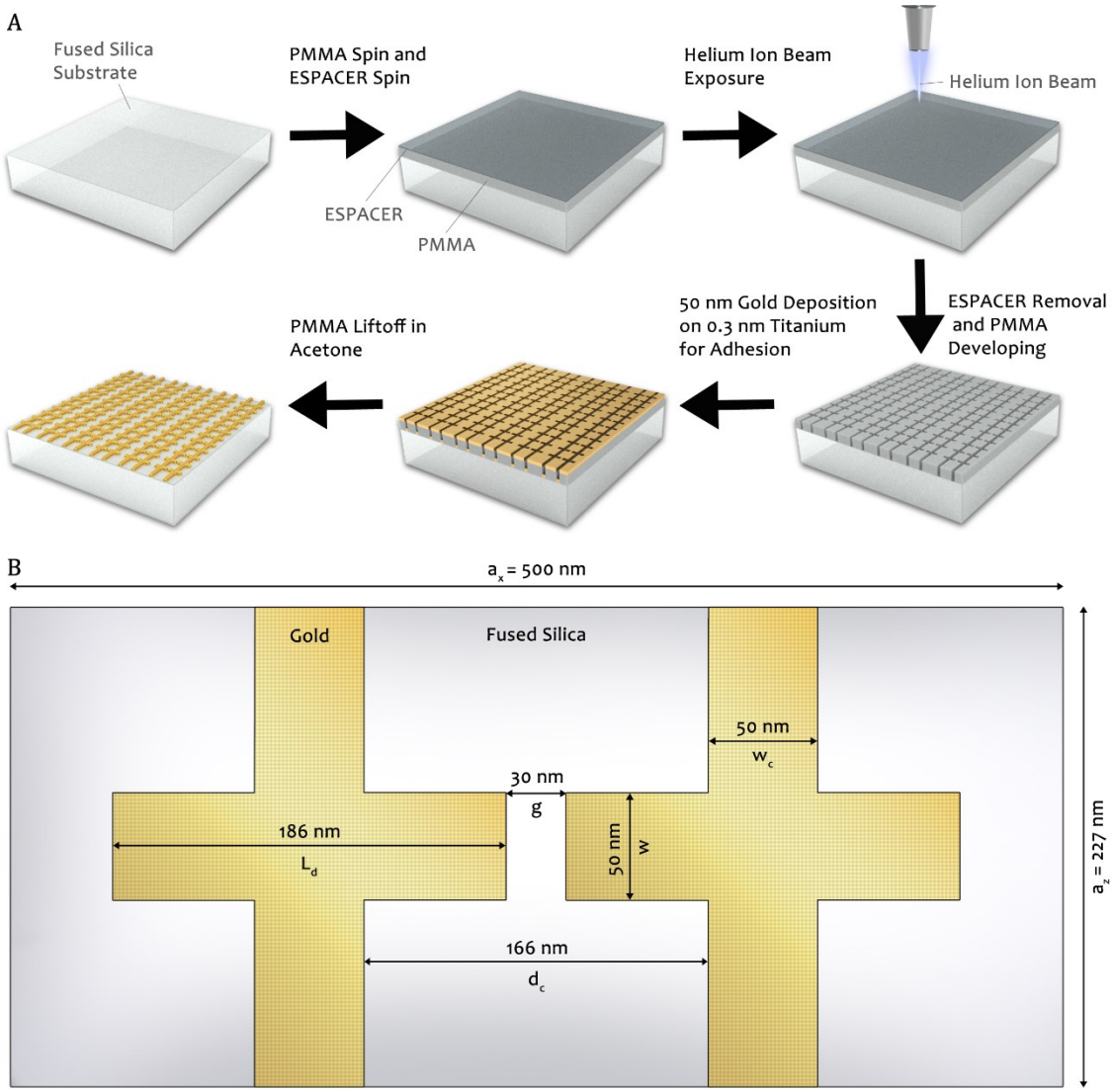

Figure 1. (A) Schematic of the fabrication process flow for patterning gold nanoantenna arrays with helium ion beam lithography and liftoff using PMMA resist. ESPACER 300Z application and removal process steps could be eliminated if the substrate is conductive. (B) Sketch in top view of the unit cell comprising the nanoantenna array of interest, along with target dimensions. L_d: nanoantenna arm length; w: nanoantenna arm width; g: nanoantenna dipole gap; w_c: connector width; d_c: connector position; a_x: unit cell length; a_z: unit cell width. Electrical contacts run through the center of each arm of the dipole nanoantenna.

Fabrication of nanoantenna arrays

The nanofabrication process flow is illustrated in Figure 1A. A fused silica substrate is cleaned by submerging it in an acetone bath and sonicating it at 37 kHz and 80% power for 5 minutes, followed by another bath of isopropanol (IPA) at the same sonication settings for the same amount of time to dissolve organic contaminants. The substrate is then rinsed with IPA, dried with nitrogen, and baked at 200 °C for 10 minutes to dehydrate. PMMA resist (950k molecular weight, 4 wt % in anisole, purchased from Kayaku Advanced Materials, Inc.) is dispensed on the substrate with a saturation time of 20 seconds, then spin-coated as described in Table A of the supplementary information document. The PMMA film is then baked at 180 °C for an hour to remove residual anisole. ESPACER 300Z (purchased from SHOWA DENKO K.K.), used to dissipate charge accumulation, is dispensed onto the substrate with a saturation time of 1 minute, and spin-coated as described in Table A of the supplementary information document.

The nanoantenna arrays are patterned in the PMMA resist with the Zeiss Orion NanoFab HIM, following the process flow sketched in Figure 1A. The layout was generated with the Fibics NanoPatterning and Visualization Engine (NPVE). A helium probe is set at a landing energy of 25 kV, spot control of 6 to move the beam crossover position up in the column which results in a lower beam current, an aperture size of 5 μm, and a relatively low helium gas pressure depending on the value of the best imaging voltage (BIV) required to achieve a beam current of 68-98 fA. The BIV corresponds to the extraction field that results in the highest ionization rate of helium at the trimer and hence the maximum beam current. The BIV value varies as the trimer ages. Spot control is a value from 1 to 10 corresponding to the beam crossover position in the column. Spot 1 gives the maximum current since the crossover is positioned at the aperture allowing passage of the full beam. Though the beam current lies below the minimum specification of the operating

beam current of the instrument (0.1 pA), it is believed that the beam current itself is stable and the measurement is affected by the limit of detection of the Faraday cup. This is evident by the repeatability of the patterned structures, observed over 30 iterations. Working with such a low beam current (68-98 fA) is a mainstay of this process, since a higher beam current, *e.g*. 0.2 pA, causes over-exposure and severely rounded final structures. Beam alignment and stigmation is performed at a beam current of 0.5 pA then the helium gas pressure is lowered to achieve the 68-98 fA beam current without the need to re-align the beam. A beam current value of 80 fA, corresponding to the average of the measured value, is assigned on the NPVE software prior to specifying the exposure parameters.

The exposure parameters used to define the nanoantenna arrays are: beam step size of 2 nm, dwell time of 4.5 μs, and an area delivered dose of 9 $\mu C/cm^2$ as listed in Table 1. The helium beam is focused at a working distance of approximately 8 mm. Post-exposure, the substrate is then placed in a bath of deionised (DI) water for 2 minutes to remove ESPACER 300Z, rinsed with DI water, and dried with nitrogen. PMMA is subsequently developed in a mixture of methyl isobutyl ketone (MIBK):isopropanol (IPA) in a ratio of 1:3 for 2 minutes at 20 °C, followed by a 30-second bath in IPA to stop PMMA from further developing. The substrate is rinsed with IPA and dried with nitrogen.

A 50 nm thick gold layer is then thermally evaporated (Angstrom Engineering NEXDEP physical vapor deposition system) at a rate of 0.05 nm/s onto a 0.3 nm thick titanium layer evaporated at a rate of 0.01 nm/s to promote gold adhesion to the fused silica substrate. The deposition process is initiated at a pressure of 3×10^{-5} Pa. The nanoantenna arrays are realised after carrying out PMMA liftoff by submerging the substrate in acetone for approximately 24 hours at room temperature. Doped Si was also used as a substrate with no alteration to the process, except

eliminating the ESPACER 300Z application and removal steps (ESPACER is not needed on a conductive substrate).

Table 1. Helium ion beam and exposure parameters for all patterns produced herein. The beam current depends on the value of the best imaging voltage (BIV), spot control, beam limiting aperture size, and pressure of the helium gas present in the column. In our HIM, spot control is a value ranging from 1-10, corresponding to the beam crossover position in the column. Spot 1 gives the maximum current since the crossover is positioned at the aperture allowing passage of the full beam. Beam focus and alignment vary with the beam parameters, except for the helium gas pressure. The beam was always focused at a working distance of approximately 8 mm. The landing energy was always kept at 25 kV.

Structure	Spot Control	Aperture size (μm)	Measured Beam current (pA)	Assigned beam current in NPVE (pA)	Beam step size (nm)	Dwell time (μs)	Passes	Dose
10×10 μm^2 nanoantenna array	6	5	0.068-0.098	0.083	2	4.5	1	9 $\mu C/cm^2$
Contact lines through nanoantenna array	6	5	0.068-0.098	0.083	0.5	0.1	4	14 $\mu C/cm^2$
20 × 20 μm^2 area of exposed PMMA for Raman spectroscopy	4	10	1.5	1.5	2	1.2	1	12 $\mu C/cm^2$
Microstructures to determine PMMA thickness	4	10	1.5	1.5	0.25	0.3	1	12 $\mu C/cm^2$
14 nm wide isolated single-pixel lines	6	5	0.068-0.098	0.083	2	26	1	12 pC/cm
18 nm wide isolated single-pixel lines	6	5	0.068-0.098	0.083	2	32	1	15 pC/cm
50% duty cycle line/space gratings, 60 nm pitch	6	5	0.068-0.098	0.083	2	3.5	1	7 $\mu C/cm^2$
50% duty cycle line/space gratings, 100 nm pitch	6	5	0.068-0.098	0.083	2	4	1	8 $\mu C/cm^2$

Overlays with photolithographic microstructures

Gold fan-out microstructures, of total thickness 38 nm (35 nm gold on 3 nm titanium), were fabricated on a 2-inch fused silica wafer using a UV lithography and liftoff process.[21] This wafer

was cleaned as previously described, then PMMA resist (950k molecular weight, 4 wt % in anisole) and ESPACER 300Z were spin-coated as described above and in Table A of the supplementary information document. PMMA was baked in the same manner as described above, prior to the application of ESPACER 300Z.

HIM imaging quality through a PMMA layer is poor and our instrument is not equipped with a precision translation stage (*e.g.*, controlled via laser interferometry). Thus, electron beam imaging (which is effective through PMMA), electron beam exposure, and development steps were applied to clear PMMA from gold alignment marks on the wafer, which must be visible for overlay alignment in the HIM. Opening of the alignment marks was carried out using a Raith Pioneer e-beam lithography system as described in the supplementary information document. The cleared alignment marks include a label to identify the device number on the wafer, a circular structure that is 1100 μm away from the label, an alignment mark that is 900 μm away from the circular structure and 100 μm away from the region of interest to be patterned by HIM. After loading the sample into the HIM chamber, the stage was driven to image these features in sequence and position the region of interest in the middle of the field of view (FOV).

The nanostructure patterned in the region of interest consisted of a nanoantenna array with 40 electrical contacts routed to the pre-existing gold fan-out structure defined using UV lithography. A write field of 50 μm was used to pattern firstly the nanoantenna array and its perpendicular contacts (Figure 1B), then route the contacts to the fan-out structure. The exposure parameters used are found in Table 1. The write-time of the array and the 40 contacts was 2 minutes and 30 seconds. The ESPACER 300Z removal, PMMA development, gold deposition, and PMMA liftoff process steps remain unchanged. The sample was then coated by a 5 nm thick conformal

layer of alumina (Al_2O_3) via atomic layer deposition (NaMLab, Germany) to passivate and protect the structure during optical characterization.

Fabrication of isolated single-pixel lines and line-space gratings

Two Si substrates were cleaned similarly to the fused silica substrate as described above. PMMA 950k molecular weight, 4 wt % in anisole was spin-coated and baked on one of the substrates and PMMA 950k molecular weight, 2 wt % in anisole was spin-coated and baked on the other substrate resulting in PMMA thicknesses of 133 and 70 nm, respectively. Both spins were carried out using the PMMA spin parameters in Table A of the supplementary information document, then baked at 180 °C for an hour. Arrays of isolated single-pixel lines, 10 μm in length and separated by 100 nm, were patterned in the PMMA using the exposure parameters given in Table 1. A line dose gradient was applied to the isolated single-pixel lines to identify the dose that fully clears the PMMA and results in the smallest linewidth possible.

In addition to arrays of isolated single-pixel lines, line-space gratings, of duty cycle 50%, of pitch 20, 40, 60, 80 and 100 nm, and of length 5 μm were patterned in the PMMA. Detailed exposure parameters of the smallest successfully fabricated gratings can be found in Table 1. The substrates were then developed in the same way as the fused silica substrates. 50 nm of gold was then deposited on 0.3 nm of titanium by thermal evaporation on the substrate bearing the 133 nm-thick PMMA, and 20 nm of gold was deposited on 0.3 nm of titanium on the substrate bearing the 70 nm-thick PMMA (the same deposition rates used for the nanoantenna arrays were also used here). The PMMA on both wafers then underwent the same liftoff process as previously described.

Fabrication of structures for Raman scattering of exposed PMMA

Raman spectra collected from PMMA exposed to the helium ion beam are expected to elucidate the nature of the chemical changes that are produced in PMMA due to exposure. A Si substrate was cleaned similarly to the fused silica substrate described above. Then a 100 nm thick layer of silver was thermally evaporated at a rate of 0.1 nm/s on a 10 nm thick film of titanium evaporated at a rate of 0.05 nm/s. PMMA was then spin-coated and baked onto the silver surface as described in Table A of the supplementary information document. A silver layer was used below the PMMA to isolate observation of PMMA Raman peaks only (without interference from substrate peaks). A 20×20 μm^2 square was patterned in the PMMA with a dose of 12 $\mu C/cm^2$ to perform Raman scattering measurements on exposed PMMA for comparison to non-exposed PMMA. Detailed exposure parameters are found in Table 1.

Results and Discussion

Raman spectra of exposed and non-exposed PMMA

The sample prepared to acquire Raman spectra, consisting of exposed and non-exposed PMMA on silver on titanium, was imaged using a Witec Alpha a300 Raman microscope in the back-scattering configuration using a laser source of wavelength $\lambda_0 = 532$ nm and a power output of 30 mW focused through an objective lens with a magnification of 20× and a numerical aperture of 0.4. The photons scattered by the sample are dispersed by a 600 groove/mm grating providing a resolution of approximately 4 cm^{-1} within the spectrograph. A background subtraction was applied to the spectra using Origin data analysis software. The assignment of Raman peaks in the exposed PMMA and non-exposed PMMA spectra was carried out following the litterature.[22–26]

The Raman spectra of non-exposed PMMA, and of PMMA exposed with the helium ion beam are shown in Figure 2 as the black and blue curves, respectively. The peak at a Raman shift of 603 cm^{-1} is attributed to stretching of the ester group in PMMA. Its intensity decreases with exposure by the helium ion beam due to cleavage of the C-C bond resulting in the abstraction of the ester group.[23] Consequently, a reduction in peak intensity is observed at Raman shifts of 815, 996 and 1736 cm^{-1}, due to stretching of the single-bonded oxygen in C-O-C, rocking of the O-CH_3 bond, and stretching of C=O bonds in the ester group, respectively. The peak at a Raman shift of 1450 cm^{-1}, originating from C-H stretching of CH_3 in the ester side group and the other methyl group in PMMA, also experiences a reduction in intensity. These intensity declines, due to helium ion beam exposure, indicate the disassociation of the ester group. Thus, PMMA undergoes main-chain scission resulting in the emergence of the stretching vibration of C=C at 1640 cm^{-1}, which is also ascribed to the presence of methyl methacrylate (MMA) monomer (as observed in other studies during PMMA polymerization[24]). This peak is conspicuously absent on the spectrum of the non-exposed PMMA in Figure 2. Thus, irradiating PMMA with a helium ion beam causes polymer degradation, which allows the developer to dissolve the exposed regions of PMMA, enabling the positive tone behaviour of PMMA. Full Raman spectra (from 250 to 3500 cm^{-1}) along with peak assignments for both non-exposed PMMA and exposed PMMA can be found in Figure S1 and Table B of the supporting information document.

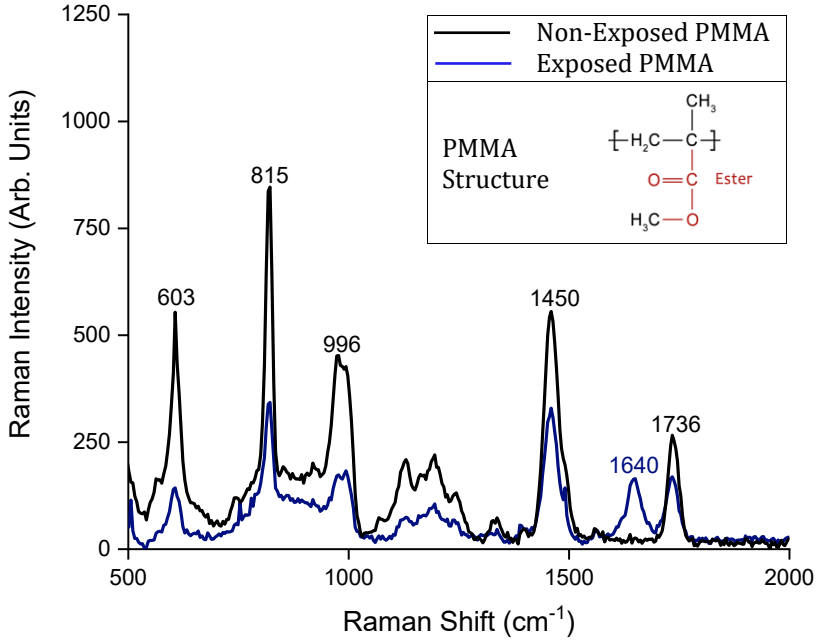

Figure 2. Raman spectra of non-exposed PMMA (black), and of PMMA exposed by a helium ion beam to a dose of 12 μC/cm^2 (blue). The PMMA molecular structure is shown in the insert. Upon exposure, PMMA undergoes main-chain scission resulting in the emergence of a C=C peak at a Raman shift of 1640 cm^{-1}.

Patterned and developed PMMA

Figure 3A shows an AFM scan of microstructures in PMMA patterned with a helium ion beam current of 1.5 pA and a dose of 12 μC/cm^2 (detailed exposure parameters are found in Table 1), and developed as described above. The root-mean-square roughness, R_q, of the substrate and PMMA layer are 0.5 and 0.7 nm, respectively, taken over the areas highlighted in red on Figure 3A. Figure 3B shows the thickness profile of the microstructures patterned in PMMA, from which a PMMA thickness of 133 nm is measured. The process has been successfully applied to PMMA layers of various thicknesses, up to 200 nm, on different substrates. The AFM images of developed PMMA were obtained in tapping mode using a Park Systems NX10 atomic force microscope (AFM) with a Tap300Al-G tip from NanoAndMore.

Figure 3C shows a nanoantenna array patterned in PMMA post-development, imaged with the HIM to evaluate the exposure quality prior to further processing. It should be noted that HIM imaging of PMMA in this manner may be destructive, as the helium imaging beam also exposes the PMMA. In addition, Figure S2 in the supporting information document shows a HIM image of Tabaret and Desmarais Halls at the University of Ottawa, in exposed and developed PMMA, as an example of complex large-area HIBL - sub 20 nm features are resolved on this pattern even though a write-field of 150 μm was used to define the image.

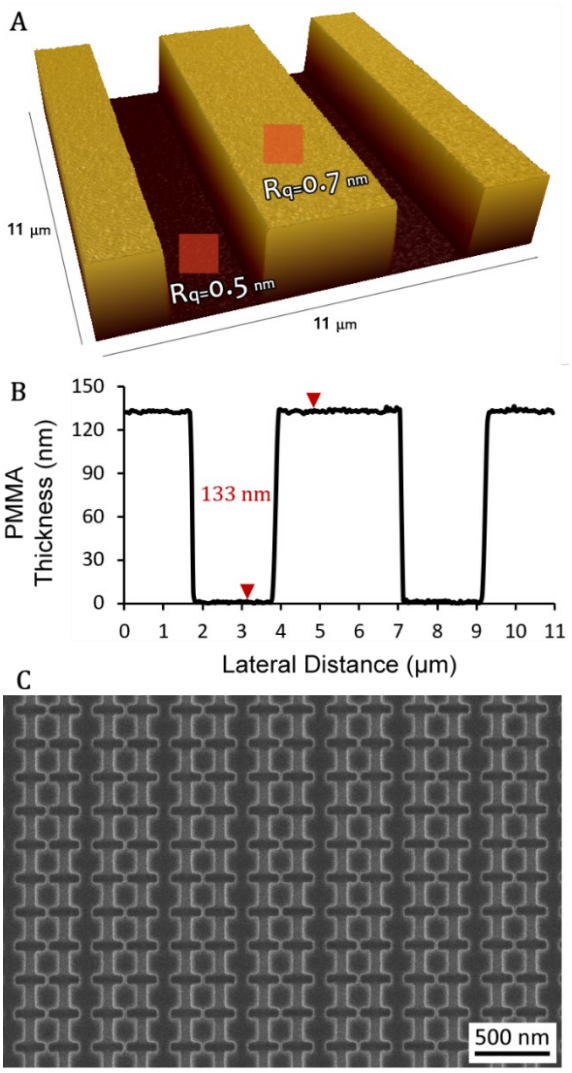

Figure 3. (A) AFM scan of developed microstructures in PMMA on silicon. These structures were patterned with a helium ion beam current of 1.5 pA and a delivered dose of 12 μC/cm^2. (B) PMMA thickness profile of the developed microstructures gives a step height of 133 nm. (C) Helium ion

microscope image of a developed nanoantenna array on a silicon substrate, used to evaluate the quality of the pattern prior to further processing.

Nanoantenna arrays

Gold nanoantenna arrays were realised as described in the previous section. Figure 4A shows a HIM image of a nanoantenna array on a silicon substrate post liftoff. The layout used for exposure is superimposed on the image in red outline, revealing good overall dimensional agreement. Figure 4B shows a zoomed-in image of the nanoantenna array, revealing that all measured dimensions are within 1 - 2 nm of the target dimensions on the layout (Figure 1B). Proximity effects are not evident, precluding the need for proximity effect mitigation. The roundness of the rectangular nanoantenna structures is evaluated by measuring the radius of curvature of several corners, which works out on average to 9 ± 2 nm (an example measurement of the radius is shown in Figure 4B).

Figure 4C shows an AFM scan of the same gold nanoantenna array but fabricated on a fused silica substrate. The root-mean-square roughness, R_q, of the substrate and gold nanoantenna array are found to be 0.3 and 1.7 nm, respectively, on the regions highlighted in red on Figure 4C. Figure 4D shows a thickness profile measured across two contact lines between nanoantennas, following the white path traced on Figure 4C. Thickness profile shows a step height of 48 nm, which is slightly lower than the target thickness of 50 nm. This thickness difference is attributed to a slight drift in the tooling factor of the deposition system. These AFM images were acquired in tapping mode using a Bruker Dimension Icon AFM with a SCANASYST-AIR tip from Bruker. Figures S3A and S3B in the supporting information document show HIM images of these arrays.

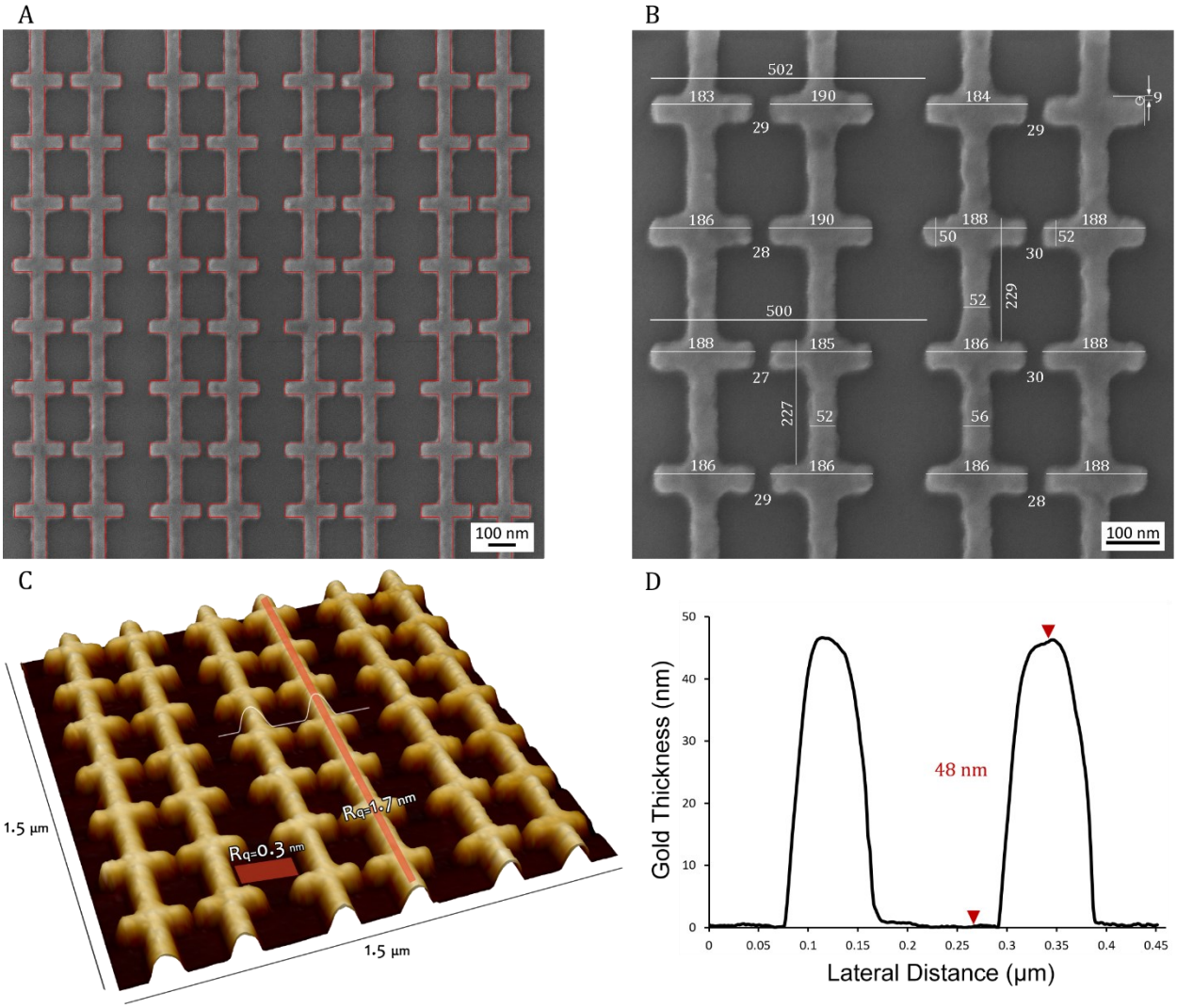

Figure 4. HIM images of a gold nanoantenna array post PMMA liftoff, (A) at a low magnification with the layout superimposed in red outline on the image, and (B) at a high magnification with feature measurements labelled in white (nm). These dimensions can be compared to those on the layout of Figure 1B. (C) AFM scan of a gold nanoantenna array, along with the roughness on the substrate and on the gold structures, obtained over the regions highlighted in red. (D) The thickness profile of the gold nanoantenna array, taken along the white trace plotted in (C), gives a step height of 48 nm. (A) and (B) nanoantennas fabricated on a silicon substrate; (C) and (D) nanoantennas fabricated on a fused silica substrate.

Overlays with photolithographic fan-out

The HIM was used to expose nanoantenna arrays and connect them to large fan-out microstructures through manual overlay alignment, as described in the previous section. The fan-out microstructures were first fabricated on a two-inch fused silica wafer via UV lithography and

liftoff.[21] The narrowest of these microstructures are 1.3 μm wide fingers converging toward a central area destined to bear a nanoantenna array.

Figure 5 shows a HIM image of a 10 × 10 μm^2 gold nanoantenna array positioned in this area, and for which each column is connected to a finger of the fan-out microstructure (since the substrate is fused silica, the electron flood gun was used during imaging to neutralise charging of the substrate). Forty nanoscale connections were established to forty fan-out fingers in this manner. The thickness of the gold nanoantennas and connections (50 nm) is larger than that of the fan-out fingers (38 nm) thereby ensuring good step coverage at the connection point, as revealed by the high-magnification image acquired at a stage tilt of 54° shown in inset.

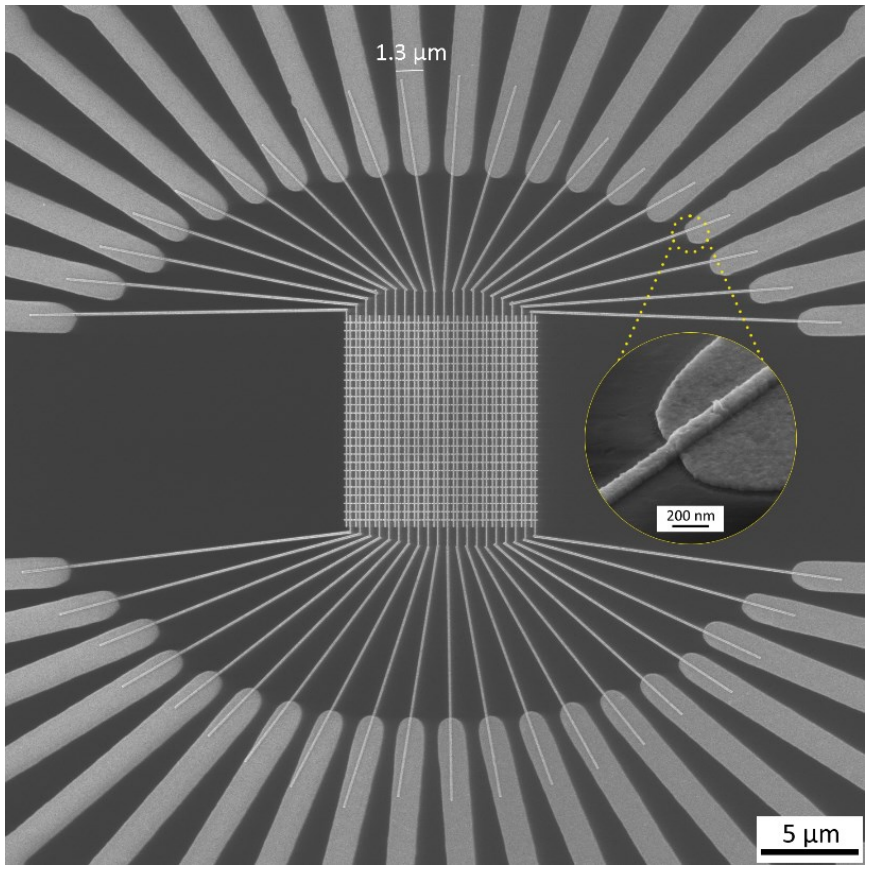

Figure 5. HIM image taken with an electron flood gun demonstrating overlay alignment of a 10 × 10 μm^2 gold nanoantenna array and its connections to 40 gold fingers of a fan-out microstructure. Inset: Magnified image acquired at a tilt angle of 54° reveals step-height coverage of a fan-out finger by a nanoscale connector. The structures were fabricated on a fused silica substrate.

Resolution tests

Isolated single-pixel lines and line-space gratings were fabricated as described in the previous section. Figure 6A shows arrays of isolated single-pixel lines where the helium ion beam dose was increased from left to right. The smallest widths of isolated single-pixel lines obtained on these samples is 14 nm for a gold/titanium thickness of 20 nm patterned in 70 nm thick PMMA with a line dose of 12 pC/cm, and 18 nm for a gold/titanium thickness of 50 nm patterned in 133 nm thick PMMA with a line dose of 15 pC/cm, as shown in Figures 6B and 6C. These widths and thicknesses, yield aspect ratios of 1.4:1 and 2.8:1, respectively. These aspect ratios are larger than the largest reported ratio of 0.7:1 produced with a 100 kV electron beam system exposing a 40 nm thick PMMA layer with proximity correction and cold development at -15 °C, followed by evaporating a 10 nm thick titanium film and PMMA liftoff.[20]

A 50% duty cycle line-space grating of pitch 60 nm, having a gold/titanium thickness of 20 nm, fabricated using a dose of 7 μC/cm^2 on 70 nm thick PMMA, is shown in Figure 6D, along with the measured dimensions of the lines and spaces (nm). A 50% duty cycle line-space grating of pitch 100 nm, having a gold/titanium thickness of 50 nm, fabricated using a dose of 8 μC/cm^2 on 133 nm-thick PMMA, is shown in Figure 6E. Line-space gratings (50% duty cycle) of 20 and 40 nm pitches were not resolved in 70 nm thick PMMA, whereas pitches of 60, 80 and 100 nm were successfully resolved. Line-space gratings (50% duty cycle) of 20, 40, 60 and 80 nm pitches were not resolved in 133 nm thick PMMA, but a 100 nm pitch was successfully resolved.

Resolution failure was partly due to PMMA delamination around the line-space gratings of smaller pitches. In a subsequent trial, the PMMA was diluted and spin-coated to a thickness of 43 nm, and baked at 180 °C for an hour. The PMMA film was then subjected (additionally) to a pre-exposure bake of 3 minutes at 180 °C. These changes resulted in the liftoff of line-space

gratings with a 50% duty cycle, of 40 nm pitch, with a gold/titanium thickness of 20 nm patterned with a dose of 2.5 $\mu C/cm^2$ (Figure 6F).

Nanostructures were also fabricated on insulating magnesium oxide (MgO) substrates and on a silver film deposited onto a doped Si substrate (results not shown) with minimum alterations to the process.

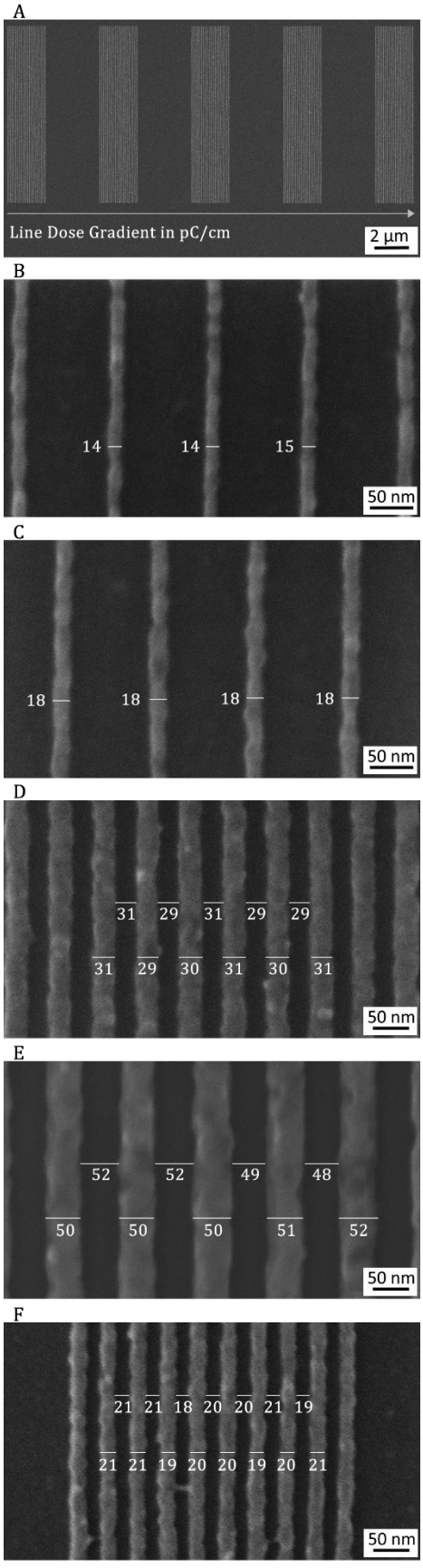
A
Line Dose Gradient in pC/cm
2 µm
B
14
14
15
50 nm
C
18
18
18
18
50 nm
D
31 29 31 29 29
31 29 30 31 30 31
50 nm
E
52 52 49 48
50 50 50 51 52
50 nm
F
21 21 18 20 20 21 19
21 21 19 20 20 19 20 21
50 nm

Figure 6. (A) Arrays of line doses to define isolated single-pixel lines, increasing left to right from 11 pC/cm to 15 pC/cm in steps of about 1 pC/cm (the dwell time was varied from one array of isolated lines to another by 2 μs). (B) 14 nm wide isolated lines, fabricated using 70 nm thick PMMA patterned with a dose of 12 pC/cm, and 20 nm thick gold on 0.3 nm titanium. (C) 18 nm wide isolated lines, fabricated using 133 nm thick PMMA patterned with a dose of 15 pC/cm, and 50 nm gold on 0.3 nm titanium. (D) 60 nm pitch, 50% duty cycle line-space gratings, fabricated using 70 nm thick PMMA patterned with a dose of 7 $\mu C/cm^2$, and 20 nm gold on 0.3 nm titanium. (E) 100 nm pitch, 50% duty cycle line-space gratings, fabricated using 133 nm thick PMMA patterned with a dose of 8 $\mu C/cm^2$, and 50 nm gold on 0.3 nm titanium. (F) 40 nm pitch, 50% duty cycle line-space gratings, fabricated using 43 nm thick PMMA patterned with a dose of 2.5 $\mu C/cm^2$, and 20 nm gold on 0.3 nm titanium. All structures were fabricated on silicon substrates. The dimensions labelled in white are in nm.

Transmittance responses of nanoantenna arrays

Several fabricated nanoantenna arrays were characterised optically, and compared with modelling results, to further validate the fabrication processes. The optical set-up constructed to characterise the nanoantennas makes use of a supercontinuum source and a spectrograph, as described in the supplementary document and shown in Figure S4 therein. The transmittance response of an array was taken as the ratio of its transmitted spectrum as measured on our spectrograph to that of a blank (clear) region on the same fused silica wafer. Figure 7 shows the experimental transmittance responses of five $10 \times 10\ \mu m^2$ gold nanoantenna arrays of identical target dimensions (Figure 1B), on a fused silica substrate, coated conformally with 5 nm of alumina. The five arrays produce responses that overlap very well indicating a high degree of reproducibility in fabrication.

The measurements are compared in Figure 7 to the theoretical transmittance response which was calculated numerically via 3D finite-difference time-domain (FDTD) simulations using in-house software.[27] In the modelling, all corners and edges not touching the substrate were rounded with a radius of curvature of 10 nm. The optical parameters of gold were represented using the Drude model with two critical points,[27] fitted to the measured complex permittivity of Au[28] (53 nm case therein[28]). A conformal layer of alumina was included in the model, using the

complex permittivity extracted from in-house ellipsometry measurements. The refractive index of the fused silica substrate was taken as n = 1.45. A single unit cell was simulated assuming lateral periodic boundary conditions, and excited via a plane wave linearly polarized along the nanoantenna axis. The excitation signal was broadband to calculate the transmittance over a broad wavelength range.

To obtain the best fit to the experimental transmittance, two small changes were made to the nominal design, both consistent with fabrication tolerances. First, the distance between the connectors (d_c) was increased by about 14 nm with respect to the nominal configuration of Figure 1B. This increases the distance between the two resonant dips in the transmittance curve, following previous work [2]. Second, the thickness of the alumina layer was changed from 5 to 6 nm, which red-shifts the transmittance curves by about 10 nm. These alterations lead to excellent agreement between the five experimental responses and the theoretical one, as shown in Figure 7. The agreement was quantified by computing the mean squared error (MSE) between the experimental curves and the theoretical one, reported in the legend of Figure 7. The MSE was taken as the sum of the squared deviations between the experimental data points and the theoretical ones, divided by the number of data points. Further details of the simulation parameters are given in Table C of the supporting information document.

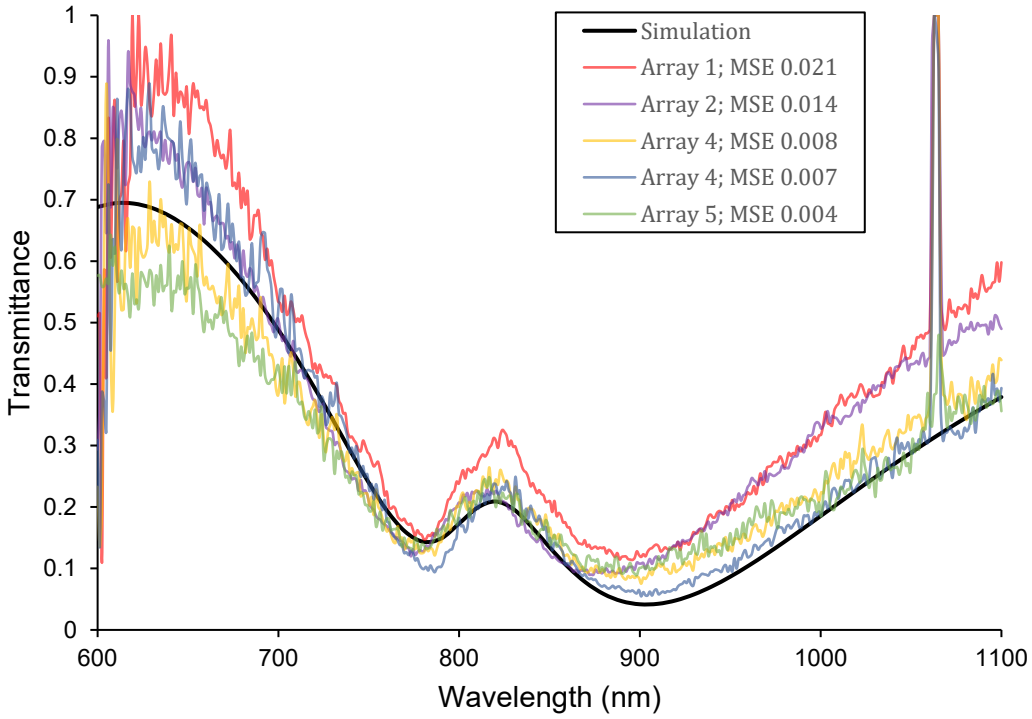

Figure 7. Normalised experimental transmittance responses of five 10 × 10 μm^2 gold nanoantenna arrays of the dimensions shown in Figure 1B, on a fused silica substrate, coated conformally by 5 nm of alumina (Arrays 1-5), along with the theoretical transmittance response calculated using the 3D FDTD method. The legend reports the mean squared error (MSE) between each measured response and the theoretical one.

Figure S5 in the supporting information document shows the normalised experimental transmittance response of a 10 × 10 μm^2 gold nanoantenna array of the dimensions shown in Figure 1B, but without the alumina layer, along with its theoretical transmittance response. The experimental response of Array 4 and the corresponding theoretical curve from Figure 7 are also plotted for comparison with the case where the nanoantenna array is coated with alumina. The shift in the resonance wavelength observed, due to coating the nanoantenna array with alumina, is 60 nm, demonstrating the high surface sensitivity of the structure and motivating its use as a biosensing structure,[1] or as an optical phased array driven by a thin charge accumulation layer.[2]

Figure S6 in the supporting information document shows the normalised experimental transmittance responses of three 10 × 10 μm^2 gold nanoantenna arrays not coated with alumina, for different gap lengths of g = 20, 30 and 40 nm. The unit cell dimensions of 500 × 227 nm^2 and the nanoantenna arm length of L_d = 186 nm were maintained constant. The responses red shift with decreasing gap length as predicted by the superimposed theoretical transmittance responses.

Conclusions

Gold nanostructures were realised by a novel helium ion beam lithography and liftoff process. Raman spectroscopy measurements on exposed PMMA confirmed the chemical transformation induced by exposure to the helium ion beam, thereby enabling subsequent development. Isolated gold lines, 20 nm thick and of width as narrow as 14 nm were fabricated, along with 50 nm thick isolated gold lines 18 nm in width, demonstrating the high resolution and high aspect ratio capabilities of the process. Dense 20 nm thick gold line-space gratings of 50% duty cycle and 40 nm pitch were fabricated, along with 50 nm thick gold line-space gratings of 50% duty cycle and 100 nm pitch. Gold nanoantenna arrays with perpendicular connections were fabricated and characterised via AFM and HIM imaging. The optical transmittance response of several nanoantenna arrays was measured, revealing a high reproducibility, and excellent agreement with theoretical responses. Finally, manual overlay alignment of nanoantenna arrays to pre-existing gold microstructures was demonstrated.

Advantageously, the process uses standard high-resolution positive tone resists developed for e-beam lithography, such as PMMA. PMMA was found to be highly sensitive to helium ion irradiation, leading to very fast patterning speeds. Importantly, proximity effects were found to be negligible, precluding the need for mitigation as generally required in e-beam lithography. The

process is transferrable with minimal alteration among conductive or insulating substrates. The process can be used to pattern any material compatible with liftoff, such as evaporated metals or dielectrics. These advantages make the process highly attractive for the realisation of nanostructures in general.

Acknowledgments

Financial support provided by Huawei Technologies Canada and the Natural Sciences and Engineering Research Council (NSERC) of Canada is gratefully acknowledged. The authors also acknowledge Dominic Goodwill and Eric Bernier from Huawei Technologies Canada for their assistance. A.C.L. acknowledges the Bundesministerium für Buldung und Furschung (German Federal Ministry of Education and Research) under the Tenure-Track Programme, and the Deutsche Forschungsgemeinschaft (DFG, German Research Foundation) under Germany's Excellence Strategy within the Cluster of Excellence PhoenixD (EXC 2122, Project ID 390833453).

References

(1) Alavirad, M.; Mousavi, S. S.; Roy, L.; Berini, P. Schottky-Contact Plasmonic Dipole Rectenna Concept for Biosensing. *Opt. Express* **2013**, *21* (4), 4328–4347. https://doi.org/10.1364/OE.21.004328.

(2) Cala Lesina, A.; Goodwill, D.; Bernier, E.; Ramunno, L.; Berini, P. Tunable Plasmonic Metasurfaces for Optical Phased Arrays. *IEEE J. Sel. Top. Quantum Electron.* **2021**, *27* (1), 1–16. https://doi.org/10.1109/JSTQE.2020.2991386.

(3) Stepanova, M.; Dew, S. *Nanofabrication Techniques and Principles*; Springer: Vienna, 2012.

(4) Alkemade, P. F. A.; Koster, E. M.; van Veldhoven, E.; Maas, D. J. Imaging and Nanofabrication With the Helium Ion Microscope of the Van Leeuwenhoek Laboratory in Delft: Imaging and Nanofabrication with a Helium Ion Microscope. *Scanning* **2012**, *34* (2), 90–100. https://doi.org/10.1002/sca.21009.

(5) Horiuchi, K.; Itakura, T.; Ishikawa, H. Fine Pattern Lithography Using a Helium Field Ion Source. *J. Vac. Sci. Technol. B Microelectron. Process. Phenom.* **1988**, *6* (1), 241–244.

https://doi.org/10.1116/1.584014.

(6) Ward, B. W.; Notte, J. A.; Economou, N. P. Helium Ion Microscope: A New Tool for Nanoscale Microscopy and Metrology. *J. Vac. Sci. Technol. B Microelectron. Nanom. Struct. Process. Meas. Phenom.* **2006**, *24* (6), 2871–2874. https://doi.org/10.1116/1.2357967.

(7) Joens, M. S.; Huynh, C.; Kasuboski, J. M.; Ferranti, D.; Sigal, Y. J.; Zeitvogel, F.; Obst, M.; Burkhardt, C. J.; Curran, K. P.; Chalasani, S. H.; Stern, L. A.; Goetze, B.; Fitzpatrick, J. A. J. Helium Ion Microscopy (HIM) for the Imaging of Biological Samples at Sub-Nanometer Resolution. *Sci. Rep.* **2013**, *3* (1), 3514. https://doi.org/10.1038/srep03514.

(8) Notte, J.; Ward, B.; Economou, N.; Hill, R.; Percival, R.; Farkas, L.; McVey, S. An Introduction to the Helium Ion Microscope. *AIP Conf. Proc.* **2007**, *931* (1), 489–496. https://doi.org/10.1063/1.2799423.

(9) Hahn, C.; Hajebifard, A.; Berini, P. Helium Focused Ion Beam Direct Milling of Plasmonic Heptamer-Arranged Nanohole Arrays. *Nanophotonics 9* (2), 393–399. https://doi.org/https://doi.org/10.1515/nanoph-2019-0385.

(10) Winston, D.; Cord, B. M.; Ming, B.; Bell, D. C.; DiNatale, W. F.; Stern, L. A.; Vladar, A. E.; Postek, M. T.; Mondol, M. K.; Yang, J. K. W.; Berggren, K. K. Scanning-Helium-Ion-Beam Lithography with Hydrogen Silsesquioxane Resist. *J. Vac. Sci. Technol. B Microelectron. Nanom. Struct. Process. Meas. Phenom.* **2009**, *27* (6), 2702–2706. https://doi.org/10.1116/1.3250204.

(11) Inai, K.; Ohya, K.; Ishitani, T. Simulation Study on Image Contrast and Spatial Resolution in Helium Ion Microscope. *J. Electron Microsc. (Tokyo).* **2007**, *56* (5), 163–169. https://doi.org/10.1093/jmicro/dfm024.

(12) Sidorkin, V.; van Veldhoven, E.; van der Drift, E.; Alkemade, P.; Salemink, H.; Maas, D. Sub-10-Nm Nanolithography with a Scanning Helium Beam. *J. Vac. Sci. Technol. B Microelectron. Nanom. Struct. Process. Meas. Phenom.* **2009**, *27* (4), L18–L20. https://doi.org/10.1116/1.3182742.

(13) Shi, X.; Prewett, P.; Huq, E.; Bagnall, D.; Boden, S. A Quantitative Comparison between Helium Ion and Electron Beam Lithography on PMMA Resist. In *42nd International Conference on Micro and Nano Engineering*; Austria, 2016.

(14) Shi, X.; Prewett, P.; Huq, E.; Bagnall, D. M.; Robinson, A. P. G.; Boden, S. A. Helium Ion Beam Lithography on Fullerene Molecular Resists for Sub-10nm Patterning. *Microelectron. Eng.* **2016**, *155*, 74–78. https://doi.org/10.1016/j.mee.2016.02.045.

(15) Luo, F.; Manichev, V.; Li, M.; Mitchson, G.; Yakshinskiy, B.; Gustafsson, T.; Johnson, D.; Garfunkel, E. Helium Ion Beam Lithography (HIBL) Using HafSOx as the Resist. In *Proc.SPIE*; 2016; Vol. 9779. https://doi.org/10.1117/12.2219239.

(16) Cattoni, A.; Mailly, D.; Dalstein, O.; Faustini, M.; Seniutinas, G.; Rösner, B.; David, C. Sub-10nm Electron and Helium Ion Beam Lithography Using a Recently Developed Alumina Resist. *Microelectron. Eng.* **2018**, *193*, 18–22. https://doi.org/https://doi.org/10.1016/j.mee.2018.02.015.

(17) Kumar, R.; Chauhan, M.; Moinuddin, M. G.; Sharma, S. K.; Gonsalves, K. E. Development of Nickel-Based Negative Tone Metal Oxide Cluster Resists for Sub-10 Nm Electron Beam and Helium Ion Beam Lithography. *ACS Appl. Mater. Interfaces* **2020**, *12* (17), 19616–19624. https://doi.org/10.1021/acsami.9b21414.

(18) Flatabø, R.; Agarwal, A.; Hobbs, R.; Greve, M. M.; Holst, B.; Berggren, K. K. Exploring Proximity Effects and Large Depth of Field in Helium Ion Beam Lithography: Large-Area Dense Patterns and Tilted Surface Exposure. *Nanotechnology* **2018**, *29* (27), 275301. https://doi.org/10.1088/1361-

6528/aabe22.

(19) Lewis, S. M.; Hunt, M. S.; DeRose, G. A.; Alty, H. R.; Li, J.; Wertheim, A.; De Rose, L.; Timco, G. A.; Scherer, A.; Yeates, S. G.; Winpenny, R. E. P. Plasma-Etched Pattern Transfer of Sub-10 Nm Structures Using a Metal–Organic Resist and Helium Ion Beam Lithography. *Nano Lett.* **2019**, *19* (9), 6043–6048. https://doi.org/10.1021/acs.nanolett.9b01911.

(20) Khiat, A.; Ayliffe, P.; Prodromakis, T. High Density Crossbar Arrays with Sub- 15 Nm Single Cells via Liftoff Process Only. *Sci. Rep.* **2016**, *6* (1), 32614. https://doi.org/10.1038/srep32614.

(21) Northfield, H.; Krupin, O.; Tait, R. N.; Berini, P. Tri-Layer Contact Photolithography Process for High-Resolution Lift-off, *Submitted*.

(22) Willis, H. A.; Zichy, V. J. I.; Hendra, P. J. The Laser-Raman and Infra-Red Spectra of Poly(Methyl Methacrylate). *Polymer (Guildf).* **1969**, *10*, 737–746. https://doi.org/https://doi.org/10.1016/0032-3861(69)90101-3.

(23) Lehockey, E. M.; Reid, I.; Hill, I. The Radiation Chemistry of Poly(Methyl Methacrylate) Polymer Resists. *J. Vac. Sci. Technol. A* **1988**, *6* (4), 2221–2225. https://doi.org/10.1116/1.575014.

(24) Pallikari, F.; Chondrokoukis, G.; Rebelakis, M.; Kotsalas, Y. Raman Spectroscopy: A Technique for Estimating Extent of Polymerization in PMMA. *Mater. Res. Innov.* **2001**, *4* (2), 89–92. https://doi.org/10.1007/s100190000076.

(25) Xingsheng, X.; Hai, M.; Qijing, Z.; Yunsheng, Z. Properties of Raman Spectra and Laser-Induced Birefringence in Polymethyl Methacrylate Optical Fibres. *J. Opt. A Pure Appl. Opt.* **2002**, *4* (3), 237–242. https://doi.org/10.1088/1464-4258/4/3/303.

(26) Thomas, K. J.; Sheeba, M.; Nampoori, V. P. N.; Vallabhan, C. P. G.; Radhakrishnan, P. Raman Spectra of Polymethyl Methacrylate Optical Fibres Excited by a 532 Nm Diode Pumped Solid State Laser. *J. Opt. A Pure Appl. Opt.* **2008**, *10* (5), 55303. https://doi.org/10.1088/1464-4258/10/5/055303.

(27) Cala Lesina, A.; Vaccari, A.; Berini, P.; Ramunno, L. On the Convergence and Accuracy of the FDTD Method for Nanoplasmonics. *Opt. Express* **2015**, *23* (8), 10481–10497. https://doi.org/10.1364/OE.23.010481.

(28) Yakubovsky, D. I.; Arsenin, A. V; Stebunov, Y. V; Fedyanin, D. Y.; Volkov, V. S. Optical Constants and Structural Properties of Thin Gold Films. *Opt. Express* **2017**, *25* (21), 25574–25587. https://doi.org/10.1364/OE.25.025574.

Supporting information document for: Helium ion beam lithography and liftoff

Sabaa Rashid,[a,b] Jaspreet Walia,[b,c] Howard Northfield,[b] Choloong Hahn,[b,c] Anthony Olivieri,[b] Antonio Calà Lesina,[d,e,f] Fabio Variola,[g] Arnaud Weck,[b,g,h] Lora Ramunno,[b,h] and Pierre Berini [b,c,h,*]

[a]Department of Chemical and Biological Engineering, University of Ottawa, 161 Louis Pasteur, Ottawa, Ontario K1N 6N5, Canada.
[b]Centre for Research in Photonics, University of Ottawa, 25 Templeton Street, Ottawa, Ontario K1N 6N5, Canada.
[c]School of Electrical Engineering and Computer Science, University of Ottawa, 800 King Edward Avenue, Ottawa, Ontario K1N 6N5, Canada.
[d]Hannover Centre for Optical Technologies, Leibniz Universität Hannover, Hannover, Germany
[e]Cluster of Excellence PhoenixD (Photonics, Optics, and Engineering – Innovation Across Disciplines), Hannover, Germany
[f]Institut für Transport- und Automatisierungstechnik, Fakultät für Maschinenbau, Leibniz Universität Hannover, Hannover, Germany
[g]Department of Mechanical Engineering, University of Ottawa, 161 Louis Pasteur, Ottawa, Ontario K1N 6N5, Canada.
[h]Department of Physics, University of Ottawa, 150 Louis Pasteur, Ottawa, Ontario K1N 6N5, Canada.

*Corresponding author: berini@eecs.uottawa.ca

Table A. PMMA and ESPACER 300Z spin parameters on Laurell WS-650-23NPP spin coater.

Layer	Step	Spin Speed (rpm)	Acceleration (rpm/s)	Duration (s)
PMMA	1	1000	100	10
	2	6000	400	15
	3	6000	0	45
	4	0	-200	30
ESPACER 300Z	1	3000	600	5
	2	3000	0	30
	3	0	-200	15

Opening of alignment marks for overlay HIBL using e-beam exposure:
Opening of the alignment marks was carried out using a Raith Pioneer e-beam lithography system. The landing energy of the electron beam was set to 10 kV through a 30 µm aperture to achieve a beam current of 200 pA. Electron beam exposure parameters were: a beam step size of 16 nm, dwell time of 2 µs, and an area delivered dose of 177 µC/cm^2. The electron beam was focused at a working distance of approximately 8 mm. After the electron beam exposure, ESPACER 300Z was removed and PMMA developed as previously described. A new layer of ESPACER 300Z was spin-coated on the PMMA anticipating exposure by the helium ion beam.

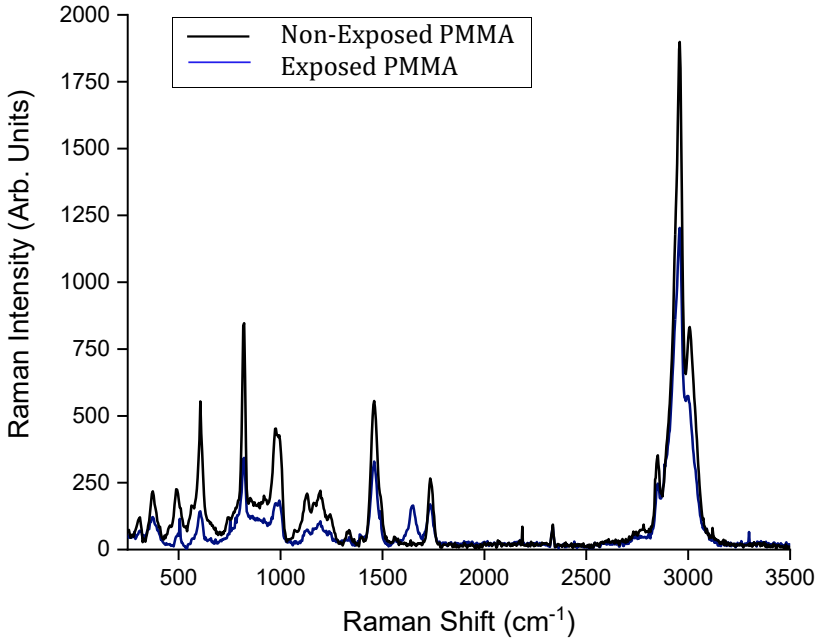

Figure S1. Raman spectra (from 250 to 3500 cm^{-1}) of non-exposed PMMA (black), and of PMMA exposed by a helium ion beam to a dose of 12 µC/cm^2 (blue). Upon exposure, PMMA undergoes main-chain scission resulting in the emergence of a C=C peak at a Raman shift of 1640 cm^{-1}.

Table B: Assignment of the observed Raman bands in Figure S1.

Raman shift reported in literature (cm^{-1})	**Raman shift (cm^{-1})**	**Assignment**
304[1]	302	Bending of C-C-C
370[1]	374	Symmetric bending of C-O and C-C in ester side group
487[1]	486	Out of plane deformation of ester side group
600[2]	603	Symmetric stretching induced in main chain of the ester group
815[2]	815	Symmetric stretching of C-O of ester side group
999[3]	996	O-CH_3 rock of the ester side group
1070-1125[2]	1070-1125	C-C skeletal stretching mode
1150-1200[2]	1150-1200	C-O stretching mode in the ester side group
1336[4]	1336	Reported but was not assigned
1395[2]	1396	C-H of CH_2 twisting mode
1450[2]	1450	C-H of CH_3 stretching induced in the CH_3 species of O-CH_3 and CH_3 in PMMA (α-CH_3)
1550[2]	1550	Ambient oxygen
1640[2]	1640	Symmetric stretching of C=C
1740[2]	1736	C=O symmetric stretching in ester side group
2848[3]	2845	Combination band involving O-CH_3
2957[3]	2957	Symmetric stretching of C-H of O-CH_3, CH_3 group in PMMA (α-CH_3), and asymmetric stretching of CH_2
3001[3]	3008	Asymmetric stretching of C-H of O-CH_3 and the other CH_3 group in PMMA C-CH_3

Figure S2. HIM image of Tabaret Hall (with Desmarais Hall in the background) at the University of Ottawa, patterned in PMMA on a silicon substrate, then developed. A helium ion beam current of 1.5 pA was used to deliver a dose of 8 μC/cm^2. Dark grey is PMMA and light grey is silicon. Sub-20 nm features are resolved on this pattern. A write-field of 150 μm was used to define the image. (Photograph courtesy of Bonnie Findley, University of Ottawa.)

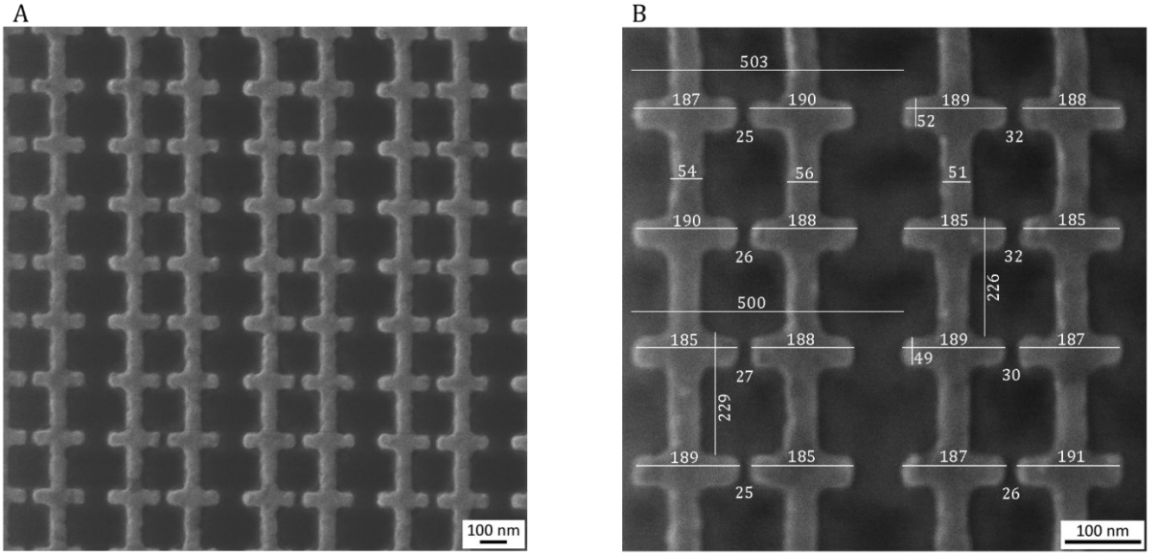

Figure S3. HIM images taken with an electron flood gun of a gold nanoantenna array on a fused silica substrate post PMMA liftoff, (A) at a low magnification, and (B) at a high magnification with feature measurements labelled in white (nm). These dimensions can be compared to those on the layout of Figure 1B.

Experimental set-up for the optical transmittance measurements:
Figure S4 shows the setup constructed to measure the optical transmittance response of nanoantenna arrays. The supercontinuum source (NKT Photonics, SuperK Extreme), emitting light covering the wavelength range from λ_0 = 410 to 2400 nm, passes through 2 neutral density filters providing attenuation to avoid damaging the setup components and nanoantenna array under test. The supercontinuum beam is then polarised linearly in the x-orientation, parallel to the a_x dimension shown in Figure 1B to excite the nanoantenna array, using a polariser (Thorlabs LPNIR100-MP2). The beam is incident on and focused through the back-side of the fused silica wafer on which reside several gold nanoantenna arrays, using an objective lens with a magnification of 20× and a numerical aperture of 0.4 (Newport M-20×), after passing through a 100 μm diameter pinhole, to produce a beam size comparable to the size of one array (10 × 10 μm^2). The transmitted light is captured by an optical fiber (Ocean Insight QP600-1-UV-VIS) and delivered to an optical spectrometer (Newport OSM2-400VIS/NIR). The optical spectrometer, connected to a computer, measures spectra over the wavelength range from λ_0 = 600-1100 nm, which covers the expected resonance wavelength of the fabricated nanoantenna arrays. A 50:50 non-polarizing beam splitter cube (Thorlabs CCM1-BS014) is placed between the pinhole and the objective to direct the beam to a CCD camera (AmScope MU300) connected to a computer. A white light source is used to locate the array of interest by providing a wider field of view compared to that of the supercontinuum beam. The CCD camera is also used to monitor the supercontinuum beam size and its location on the wafer. An array of interest is then carefully aligned to the incident beam using a precision optical translation stage. A beam dump (KENTEK ABD-0.75) is used to safely absorb the energy of the unused portion of the split supercontinuum beam.

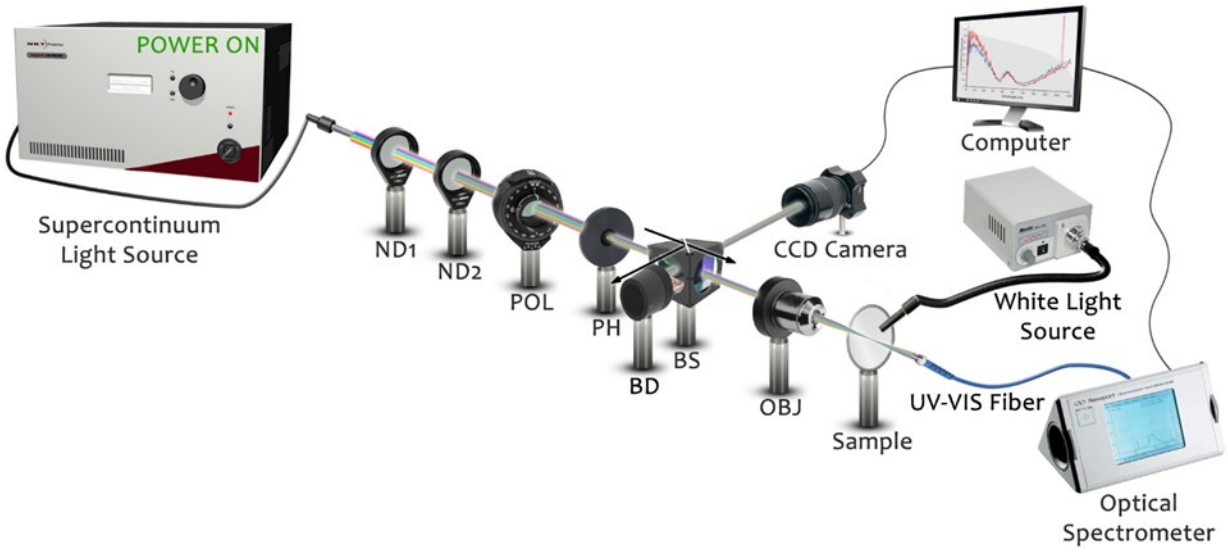

Figure S4. Optical setup built to measure the transmittance response of nanoantenna arrays fabricated on fused silica over the wavelength range from λ_0 = 600 nm to 1100 nm; ND1: neutral density filter of optical density (OD) 0.4; ND2: neutral density filter of OD 0.5; POL: linear polariser; PH: pinhole of diameter 100 μm; BS: 50:50 non-polarizing beam splitter; BD: beam dump; OBJ: 20× objective.

Table C. 3D-FDTD simulation parameters.

Simulation parameter	**Value (nm)**
Nanoantenna dipole length (L_d)	186
Nanoantenna dipole width (w)	50
Nanoantenna dipole gap (g)	30
Connector width (w_c)	50
Connectors distance (d_c)	180
Unit cell length (a_x)	500
Unit cell width (a_z)	224
Nanoantenna radius of curvature	10
Ti thickness	0.3
Au thickness	50
Alumina (Al_2O_3) thickness	6

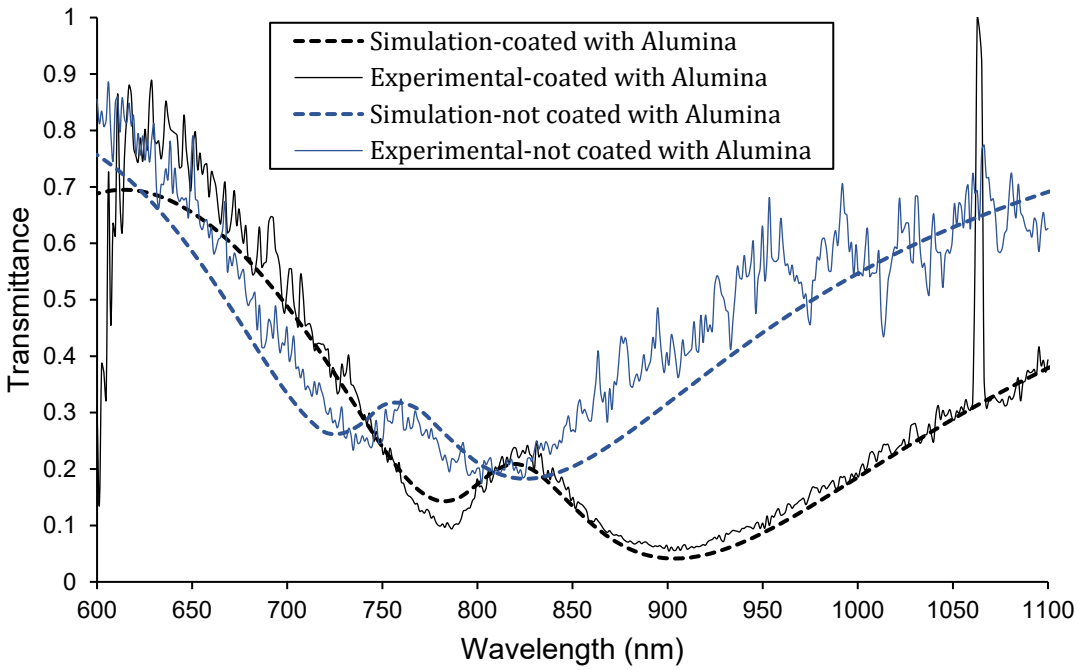

Figure S5. Normalised experimental transmittance responses of two 10 × 10 μm^2 gold nanoantenna arrays of the dimensions shown in Figure 1B. One array was coated conformally by 5 nm of alumina, and the other was not coated. The theoretical transmittance responses calculated using 3D-FDTD simulations are included. The theoretical transmittance response of the non-coated array (dashed blue) was shifted up by 0.12 to compensate for increased background light present in this measurement.

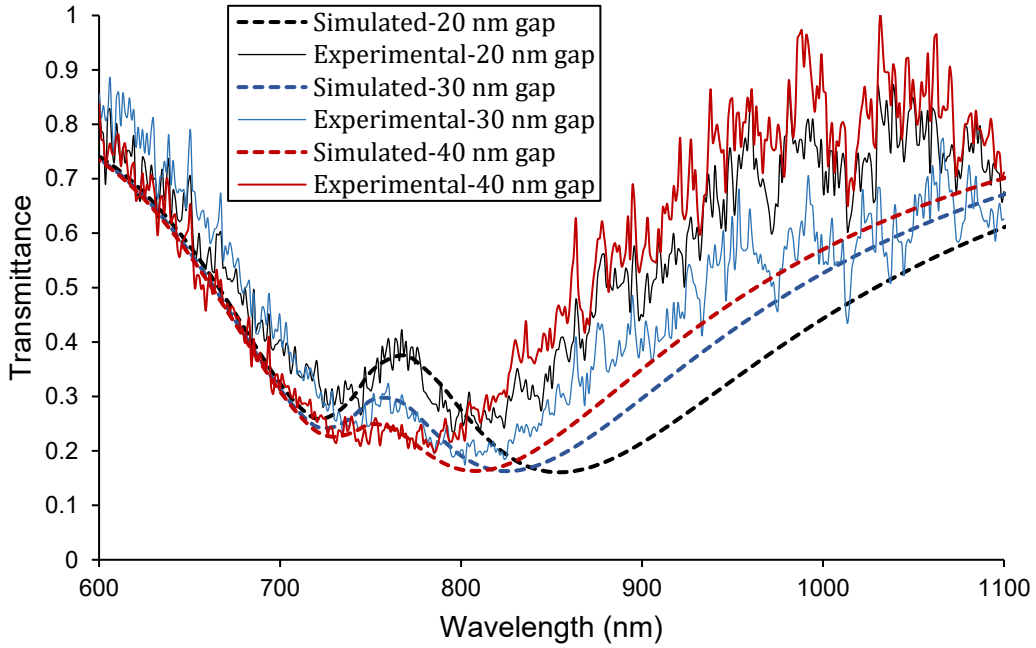

Figure S6. Normalised experimental transmittance responses of three 10 × 10 μm^2 gold nanoantenna arrays (not coated with alumina) for different gaps lengths of g = 20, 30 and 40 nm. The unit cell dimensions of 500 × 227 nm^2 and the nanoantenna arm length of L_d = 186 nm were maintained constant. The theoretical transmittance responses, calculated using 3D-FDTD simulations, were shifted up by 0.1 to compensate for background light present in this measurement.

References

(1) Willis, H. A.; Zichy, V. J. I.; Hendra, P. J. The Laser-Raman and Infra-Red Spectra of Poly(Methyl Methacrylate). *Polymer (Guildf).* **1969**, *10*, 737–746. https://doi.org/https://doi.org/10.1016/0032-3861(69)90101-3.

(2) Lehockey, E. M.; Reid, I.; Hill, I. The Radiation Chemistry of Poly(Methyl Methacrylate) Polymer Resists. *J. Vac. Sci. Technol. A* **1988**, *6* (4), 2221–2225. https://doi.org/10.1116/1.575014.

(3) Thomas, K. J.; Sheeba, M.; Nampoori, V. P. N.; Vallabhan, C. P. G.; Radhakrishnan, P. Raman Spectra of Polymethyl Methacrylate Optical Fibres Excited by a 532 Nm Diode Pumped Solid State Laser. *J. Opt. A Pure Appl. Opt.* **2008**, *10* (5), 55303. https://doi.org/10.1088/1464-4258/10/5/055303.

(4) Xingsheng, X.; Hai, M.; Qijing, Z.; Yunsheng, Z. Properties of Raman Spectra and Laser-Induced Birefringence in Polymethyl Methacrylate Optical Fibres. *J. Opt. A Pure Appl. Opt.* **2002**, *4* (3), 237–242. https://doi.org/10.1088/1464-4258/4/3/303.

3.2. Helium ion beam dose tests on PMMA

Preliminary experiments were carried out to develop a new process to transfer patterns defined by the helium ion beam in resist, but through etching the underlying layer, rather than liftoff as described in the previous Section. It is well known that irradiating PMMA by high doses causes PMMA to crosslink, thereby exhibiting a negative-tone behaviour that is useful in an etching process.

PMMA was spin-coated on a silver-titanium film on Si as described in Section *3.1.3* of this chapter. A helium ion beam dose test, where doses ranged from 1.5 to 200 $\mu C/cm^2$, was performed using a beam current of 1.5 pA on squares $20 \times 20\ \mu m^2$ in area, to track the chemical transformation of PMMA via Raman scattering measurements. Figure 3.2.1 reveals Raman spectra from 1400-1800 cm^{-1} of the tested doses. The higher the dose, the more C=C bonds formed (peak at 1640 cm^{-1}) which is consistent with results reported in literature and discussed in Section *3.1.3* of this chapter, when PMMA is exposed with radiation sources other than a helium ion beam.

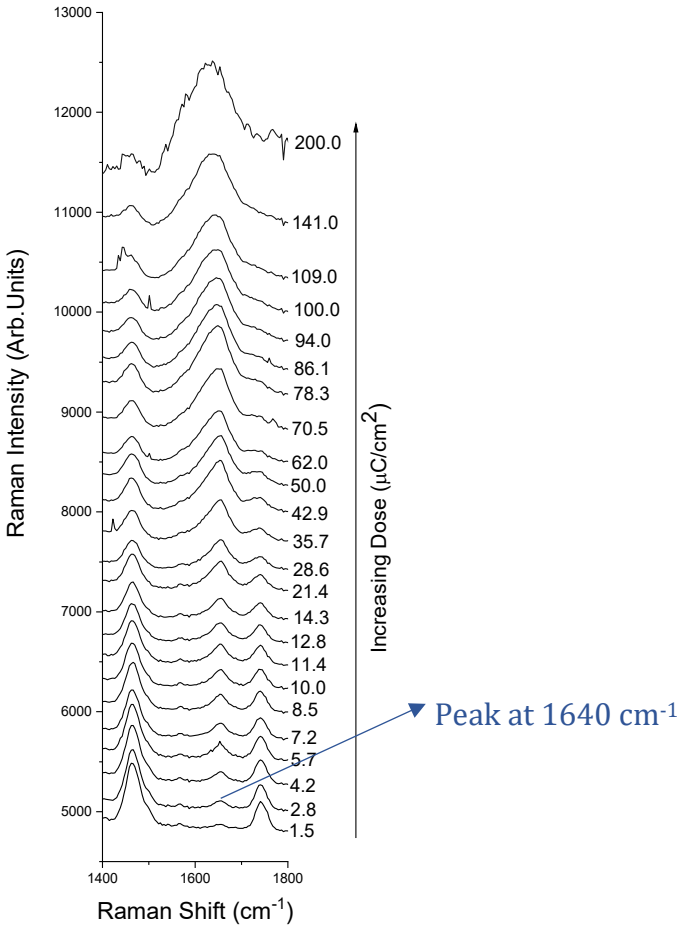

Figure 3.2.1. Raman spectra of PMMA exposed by a helium ion beam to doses from 1.5 to 200 μC/cm^2. Upon exposure, PMMA gradually undergoes main-chain scission resulting in the emergence of a C=C peak at a Raman shift of 1640 cm^{-1}. The higher the dose, the higher the intensity of this peak. Raman scattering measurements were performed by Jaspreet Walia.

The HIM images in Figure 3.2.2 show that PMMA switches to its negative-tone behaviour at a dose of ~50 μC/cm^2, when realising nanostructures of the layout depicted in Figure 3.2.2A. Figures 3.2.2B and C show nanoantenna arrays composed of crosslinked PMMA on a 30 nm-thick thermally evaporated gold film on a fused silica substrate. PMMA was exposed in B and C to doses of 40 μC/cm^2 and 50 μC/cm^2, respectively, and developed in acetone at room temperature for 5 minutes. The dimensions measured (white labelling on Figure 3.2.2C, unit of nm) are slightly

below target dimensions shown in Figure 3.2.2A. Increasing the dose would result in achieving the target dimensions. Etching the gold film and subsequently removing the mask embodied by crosslinked PMMA could lead to a process transfer of nano-scale patterns into films or substrates.

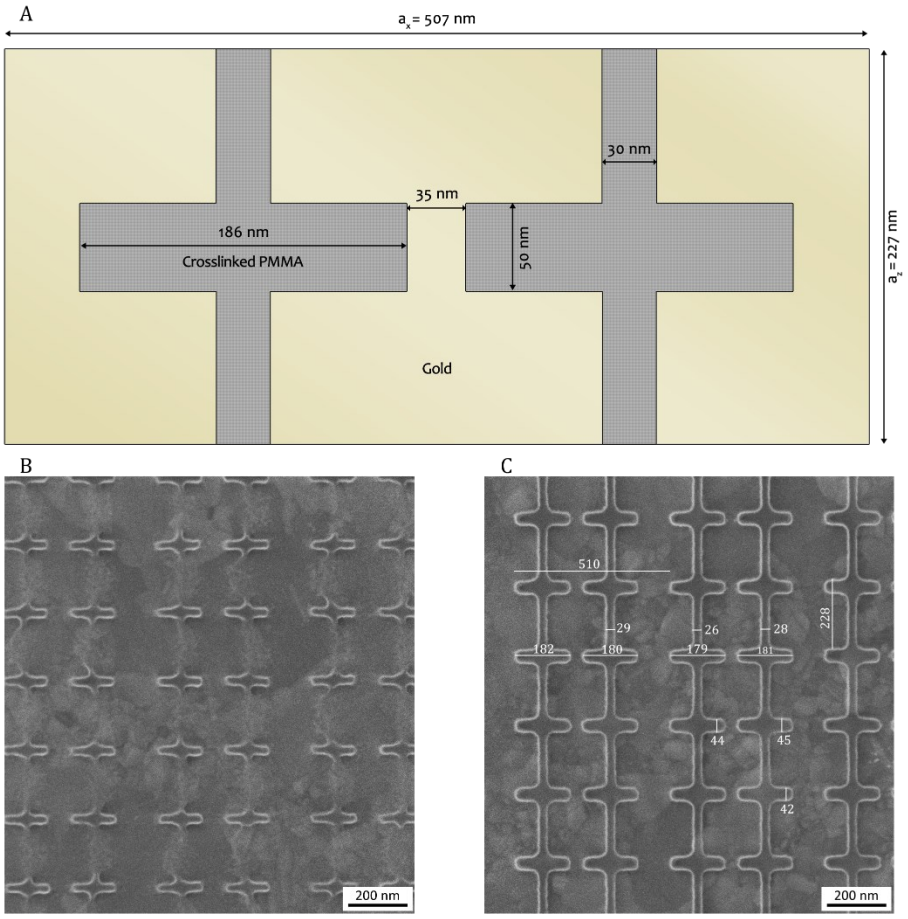

Figure 3.2.2. (A) Sketch in top view of the unit cell used for negative-tone PMMA tests comprising a nanoantenna array, along with target dimensions. The dipole nanoantenna has a gap of 35 nm and is aligned horizontally. HIM images of a nanoantenna array composed of crosslinked PMMA on a 30 nm-thick thermally evaporated gold film on a fused silica substrate. PMMA is exposed to a dose of (B) 40 μC/cm^2 and (C) 50 μC/cm^2 and developed in acetone to remove the non-exposed PMMA. Feature measurements labelled in white (nm).

Crosslinked PMMA was also exploited in patterning bitmap images of Tabaret Hall and the Advanced Research Complex of the University of Ottawa on a doped Si substrate. Sub-10 nm features were resolved despite using a large write-field of 100 μm. A beam current of 1.5 pA was

used to deliver an area dose of 150 μC/cm^2. Figures 3.2.3 and 3.2.4 show HIM images of the 2 facilities.

Figure 3.2.3. HIM image of Tabaret Hall at the University of Ottawa on Si. Dark regions are crosslinked PMMA whereas the substrate is seen on the light regions. Photograph courtesy of Bonnie Findley (University of Ottawa).

Figure 3.2.4. HIM image of the Advanced Research Complex of University of Ottawa on Si. Dark regions are crosslinked PMMA whereas the substrate is seen on the light regions.

3.3. Helium ion beam lithography on silver films

In order to demonstrate that the process described in *3.1.3* can be applied to substrates other than fused silica and doped Si, fabrication of silver gratings on a silver film was performed. The fabricated silver gratings are used in investigating photocatalytic reactions of CO_2, and its capture and storage.

A doped Si substrate was cleaned as described in Section *3.1.3* then a 100 nm thick layer of silver was thermally evaporated at a rate of 0.1 nm s^{-1} onto a 10 nm thick film of titanium evaporated at a rate of 0.05 nm s^{-1}. PMMA 950k molecular weight, 2 wt % in anisole was then spin-coated and baked onto the titanium-silver film as described in Section *3.1.3*. The PMMA thickness was measured to be 70 nm. The landing energy of the helium ion beam was set to 25 kV

through a 10 μm aperture and spot control value of 5 to achieve a beam current of 0.6 pA. Exposure parameters were: a beam step size of 2 nm, dwell time of 0.5 μs, and an area delivered dose of 8 $\mu C/cm^2$ to pattern a ~30×30 μm^2 array of 50% duty cycle gratings of pitch 470 nm (width of 235 nm and a gap of 235 nm). The helium beam was focused at a working distance of approximately 8 mm. PMMA was then developed in MIBK:IPA in a ratio of 1:3 for 2 minutes at 20 °C, followed by a 30-second bath in IPA to stop PMMA from further developing. The substrate was rinsed with IPA and dried with nitrogen. 25 nm of silver were then evaporated at a rate 0.02 nm s^{-1}. Silver gratings were realised after carrying out PMMA lift-off by submerging the substrate in acetone for approximately 24 hours at room temperature. Figure 3.3.1A shows a HIM image of the 30×30 μm^2 array and Figure 3.3.1B shows a magnified image of the gratings along with the measured dimensions in white in nm. Gratings width of 262 nm, gap of 207 nm, a pitch of 469 nm are measured, which results in a 56% duty cycle instead. A dose test is required to achieve the targeted 50% duty cycle gratings of pitch 470 nm.

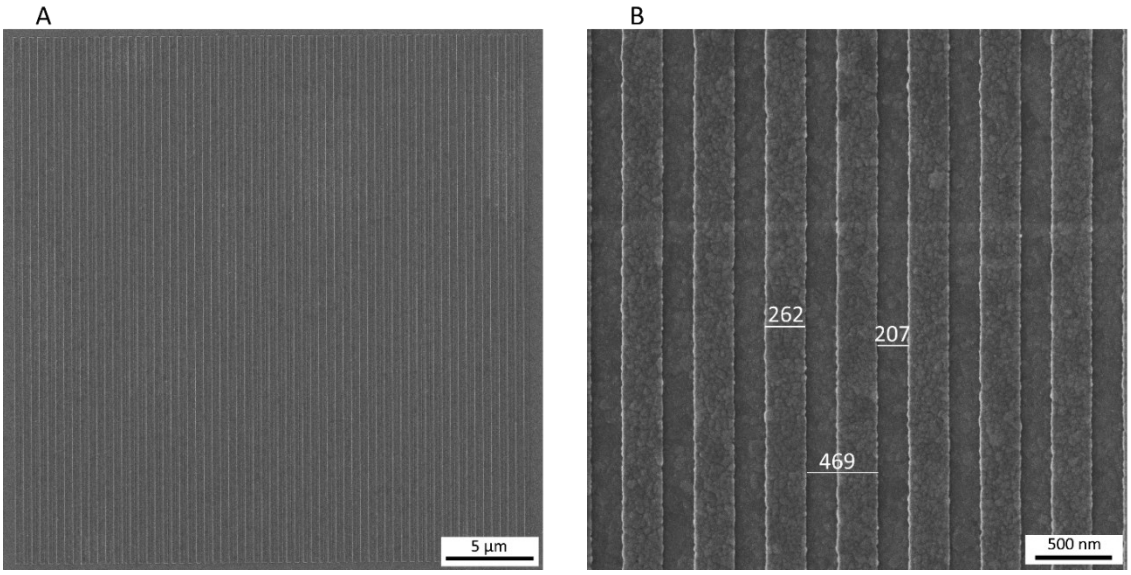

Figure 3.3.1. HIM images of a 25 nm thick silver gratings on a silver film at (A) low magnification of the 30×30 μm^2 grating area, and (B) high magnification along with the measured dimensions in white labelling (unit of nm). The measured dimensions result in a 56% duty cycle instead of the targeted 50% duty cycle.

3.4. Helium ion beam lithography on MgO substrates

In order to further demonstrate that the process described in *3.1.3* can be applied to substrates other than fused silica and doped Si, fabrication of gold gratings on an MgO substrate was performed. The fabricated gold gratings are destined to mask the substrate from an MgO etchant to transfer the gratings into the surface of the MgO substrate.

An MgO substrate was cleaned as previously described and PMMA 950k molecular weight, 2 wt % in anisole was then spin-coated on the substrate and baked, then ESPACER 300Z was spin-coated on top of the PMMA as described previously in Section *3.1.3*. ESPACER is necessary to dissipate charge accumulation on MgO. The PMMA thickness was measured to be 74 nm. Helium ion beam parameters were the same as reported in Table 2 of Section *3.1.3* and used to pattern a 10×10 μm^2 nanoantenna array. Exposure parameters were: a beam step size of 2 nm, dwell time of 2.8 μs, and an area delivered dose of 5.5 $\mu C/cm^2$ to pattern a 10 × 10 μm^2 array of 50% duty cycle gratings of pitch 64 nm (width of 32 nm and a gap of 32 nm). A dose of 5.5 $\mu C/cm^2$ was obtained by testing a gradient dose from 3-12 $\mu C/cm^2$ to determine the optimum clearing dose needed to realise the targeted dimensions. Post-exposure, the substrate was then placed in a bath of DI water for 2 minutes to remove ESPACER 300Z, rinsed with DI water, and dried with nitrogen. PMMA was subsequently developed in MIBK:IPA in a ratio of 1:3 for 2 minutes at 20 °C, followed by a 30-second bath in IPA to stop PMMA from further developing. The substrate was rinsed with IPA and dried with nitrogen. 20 nm of gold were then thermally evaporated at a rate of 0.05 nm s^{-1}. Gold gratings were realised after carrying out PMMA lift-off by submerging the substrate in acetone for approximately 24 hours at room temperature. Figure 3.4.1 shows a gold grating on MgO along with the measured dimensions (white labelling, units of

nm) which are in good agreement with the targeted ones. Since the substrate is MgO, the electron flood gun was used during imaging to neutralise charging of the substrate.

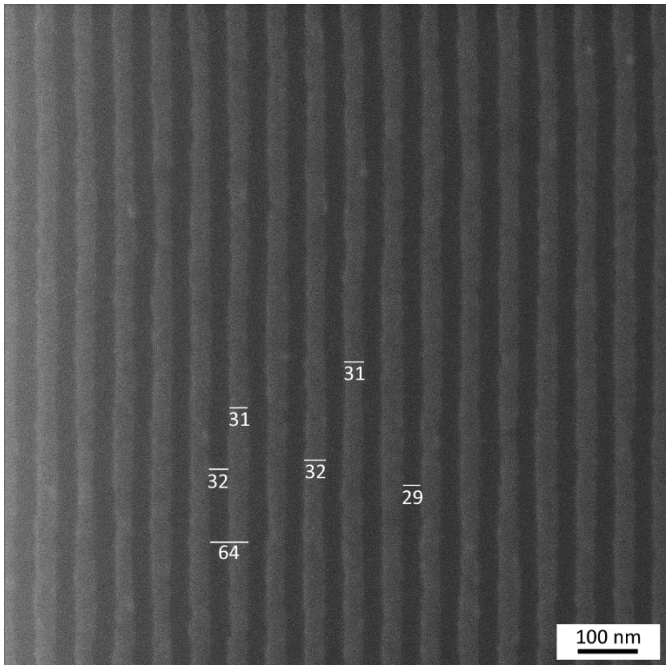

Figure 3.4.1. HIM image taken with an electron flood gun of 20 nm thick gold gratings on MgO along with the measured dimensions in white labelling (nm), which are in good agreement with the targeted dimensions of 50% duty cycle gratings of a 64 nm pitch.

Chapter 4 – Conclusions

4.1. Summary and contributions

The presented thesis outlined a study to characterise materials that are extensively used in the fabrication of biosensors (Chapter 2) and a new nanofabrication process (Chapter 3). Non-specific adsorption is a problem that adversely affects biosensors, decreasing sensitivity, specificity, and reproducibility. A number of studies are available on the non-specific adsorption of proteins to silica and SU-8; however, there were no reported data on the non-specific adsorption of proteins to the fluoropolymer CYTOP in its 3 commercially available grades that differ chemically in their terminal group. The non-specific adsorption of fluorescently-labeled BSA to these materials was studied by measuring the fluorescence intensity on the 3 grades of CYTOP (M-, A-, and S-), silica and SU-8 (Chapter 2). The fabrication process of the tested surfaces was described in addition to the microfluidic experimental setup (Chapter 2, Fig. 1). Fluorescence intensity and water contact angle results (Chapter 2, Fig. 2 and Fig. 3 (b), respectively) showed that the lowest BSA adsorption occurred on SU-8 likely due to its hydrophilicity, followed by S-grade CYTOP despite its hydrophobicity. This was ascribed to S-grade CYTOP's trifluoromethyl terminal group which resulted in lower BSA adsorption when compared to amide-silane and carboxyl terminal functional groups in M-grade and A-grade CYTOP, respectively. BSA adsorption to silica was higher than on S-grade CYTOP and SU-8 despite being hydrophilic, due to a fixed positive charge trapped in thermally grown silica on silicon and the negatively charged BSA being a in buffer with a higher pH than its isoelectric point.

A new nanofabrication process (Chapter 3, Figure 1A) was proposed and developed to fabricate nanostructures with the helium ion beam on multiple substrates including silicon, fused silica, silver and MgO, that can be used in biosensing. To fabricate the nanostructures, a clean

starting substrate is spin-coated with PMMA 950 K resist (diluted with anisole) to a thickness of up to 200 nm. Following PMMA application, the film is baked at a temperature of 180 °C on a hot plate for one hour. Then the sample undergoes exposure to the helium ion beam. Non-exposed PMMA and exposed PMMA were characterized via Raman spectroscopy to investigate the effects of the exposure. The study shows that irradiating PMMA with a helium ion beam causes polymer degradation, which then allows rapid dissolution of the exposed regions in the developer consisting of a mixture of methyl isobutyl ketone (MIBK) and isopropanol (IPA) 1:3. Following resist development, the PMMA film was then characterized using an Atomic Force Microscope (AFM) to determine the resist thickness and evaluate its surface roughness. Gold was then thermally evaporated to a thickness of up to 50 nm on the substrate, and the PMMA lifted-off with acetone to realize gold nanostructures on the substrate (Chapter 3, Figure 4). The process enabled the fabrication of 20 nm thick gold lines of width as small as 14 nm, in addition to 50 nm thick gold lines of 18 nm width on a silicon substrate (Chapter 3, Figure 6). Manual overlay alignment of nano-scale connections was successfully established to 40 fan-out microstructures that were realized through a conventional optical lithography and liftoff process, demonstrating the fabrication of a potential device with the HIM (Chapter 3, Figure 5), benefiting from negligible proximity effects and higher resist sensitivity when compared to an electron beam. Physical characterisation of fabricated nanoantenna arrays with AFM and HIM revealed good agreement with target layout dimensions. The fabrication process was further validated through optical characterisation of the nanoantenna arrays and comparison to modelling results. Excellent agreement was observed between five experimental transmittance responses measured on 5 different arrays on the same fused silica wafer, and the theoretical transmittance response that was calculated numerically via 3D-FDTD simulations (Chapter 3, Figure 7).

In addition, the nanofabrication process presented in Chapter 3 is being used in multiple projects to realise nanostructures enabling experimental testing of modelled concepts. Examples of these structures include Ag gratings on a silver film on Si and Au gratings on MgO substrate (Chapter 3, Figures 3.3.1 and 3.4.1, respectively).

4.2. Suggestions for future work

The fabricated gold nanoantenna arrays presented in Chapter 3 can be demonstrated for use as a biosensor embedded in S-grade CYTOP as a material for microfluidic channels to minimize biofouling (Chapter 2). The transmittance responses of the conformally coated nanoantenna arrays with 5 nm-thick alumina measured in (Chapter 3) in air is a demonstration of the sensitivity of the nanoantenna array as a sensor to 5 nm-thick layer of alumina when compared to the transmittance response of the gold nanoantenna array bearing no alumina layer on top (Chapter 3, Figure S5). The shift in the wavelength represents the amount of bound material to the gold structures due to the change in local refractive index. Therefore, these structures could be implemented in the fabrication of a nanoantenna array-based biosensor.

Preliminary nanofabrication tests requiring further investigations with the helium ion beam were carried out using different resists such as positive-tone resists ZEP and SML, and PMMA again but as a negative-tone resist. In addition, process optimisation is required of a tested positive-tone PMMA resist bi-layer stack, which consists of PMMA 950K on the bottom and PMMA 495K on top. Interestingly, this configuration is flipped compared to PMMA bi-layer stacks that are used in electron beam lithography, due to lower sensitivity of PMMA 495K compared to PMMA 950K to the helium beam. Such a bi-layer stack would allow the formation of an undercut and the deposition of thicker metal layers.

Appendix – Laboratory chemical safety

This appendix lists all materials that were used in this thesis. Fabrication work discussed in Chapters 2 and 3 was conducted in a clean room (Class 10,000) where coveralls, head covers, boots and gloves are always worn. Liquid chemicals were decanted in small vials that are properly labeled in a fume hood and stored in a dark well-ventilated cabinet, located in a yellow clean room, and intended for organic material storage at 22 °C unless mentioned otherwise in the table below. All the data in this table are obtained from material safety data sheets (MSDSs) supplied by the manufacturer. The reader is strongly encouraged to become familiar with the MSDS sheet of any chemical before use.

Product	Hazard data and additional storage information
CYTOP	• No adverse health effects are expected from eye and skin contact or from inhalation • If decomposed, toxic chemicals including hydrogen fluoride, carbon monoxide, perfluoro isobutylene and carbonyl fluoride are produced
SU-8	• Flammable liquid • Severe eye irritant • May cause skin eye irritation • Used under yellow light only
Bovine Serum Albumin	• Not hazardous substances or mixtures according to the manufacturer • Stored in a refrigerator at 4 °C
Phosphate buffered saline	
VectaShield mounting medium	
Poly(methyl methacrylate)	• Flammable liquid and vapour • Toxic if inhaled • Causes severe eye irritation • May cause respiratory irritation
ESPACER	• Product is not classified for health effects • Must be handled with caution because the health effects of some constitutive ingredients are not well-known • Stored in a refrigerator at 4 °C
Methyl isobutyl ketone/isopropanol (MIBK/IPA) 1:3 developer	• Highly flammable liquid and vapour • Toxic if inhaled • Causes skin and eye irritation • May cause damage to organs through prolonged or repeated contact • May cause drowsiness, dizziness, and respiratory irritation
Isopropanol	• Highly flammable liquids and vapours • Cause serious eye irritation • May cause drowsiness or dizziness
Acetone	